

# Radiation effects in $M_{n+1}AX_n$ phases

Cite as: Appl. Phys. Rev. **7**, 041311 (2020); doi: [10.1063/5.0019284](https://doi.org/10.1063/5.0019284)

Submitted: 22 June 2020 · Accepted: 30 October 2020 ·

Published Online: 7 December 2020



[View Online](#)



[Export Citation](#)



[CrossMark](#)

Chenxu Wang,<sup>1,a)</sup> Cameron L. Tracy,<sup>2</sup> and Rodney C. Ewing<sup>3,a)</sup>

## AFFILIATIONS

<sup>1</sup>State Key Laboratory of Nuclear Physics and Technology, Center for Applied Physics and Technology, Peking University, Beijing 100871, China

<sup>2</sup>Belfer Center for Science and International Affairs, Kennedy School of Government, Harvard University, Cambridge, Massachusetts 02138, USA

<sup>3</sup>Department of Geological Sciences, Stanford University, Stanford, California 94305-2115, USA

<sup>a)</sup>Authors to whom correspondence should be addressed: [cwang@pku.edu.cn](mailto:cwang@pku.edu.cn) and [rewing1@stanford.edu](mailto:rewing1@stanford.edu)

## ABSTRACT

$M_{n+1}AX_n$  phases exhibit unique laminated atomic structures that result in properties typical of both ceramics and metals. Due to their unusual characteristics, these materials have been proposed for use in a wide variety of industrial applications, including in nuclear reactors—both fission and fusion systems—where they will be exposed to extreme irradiation conditions and high temperatures. Recently, numerous studies have investigated radiation effects on the  $M_{n+1}AX_n$  phases, revealing complex behavior—phase transformations, surface modification, and mechanical property changes—induced by ion or neutron irradiation over a range of temperatures. This review summarizes recent experimental and theoretical work on the response of the  $M_{n+1}AX_n$  phases to irradiation and discusses the intrinsic controls on the radiation tolerance of these materials. Based on the review of the present body of work, a comprehensive understanding of the mechanisms of irradiation-induced structural modification and defect evolution in  $M_{n+1}AX_n$  phases is developed, as well as proposed strategies for designing novel  $M_{n+1}AX_n$  phases with enhanced performance under extreme irradiation conditions.

© 2020 Author(s). All article content, except where otherwise noted, is licensed under a Creative Commons Attribution (CC BY) license (<http://creativecommons.org/licenses/by/4.0/>). <https://doi.org/10.1063/5.0019284>

## TABLE OF CONTENTS

I. INTRODUCTION .....	2	3. Formation of an fcc-structured $(M_{n+1},A)X_n$ phase .....	7
II. STRUCTURES AND PROPERTIES OF UNIRRADIATED MAX PHASES .....	2	C. High-temperature effects on structural evolution ..	10
A. Structure .....	2	IV. COMPOSITIONAL TRENDS IN THE SUSCEPTIBILITY OF MAX PHASES TO RADIATION-INDUCED PHASE EVOLUTION .....	13
B. Key thermal, mechanical, and chemical properties .....	3	A. M atoms .....	13
1. Thermal properties .....	4	B. A atoms .....	16
2. Mechanical properties .....	4	C. X atoms .....	16
3. Chemical stabilities .....	4	D. n .....	17
III. RADIATION-INDUCED STRUCTURAL EVOLUTION IN MAX PHASES .....	4	V. PROPERTIES OF THE MAX PHASES AFTER IRRADIATION .....	19
A. Formation of M/A antisite defects .....	5	A. Mechanical properties .....	19
B. Structural evolution .....	5	B. Formation of helium bubbles .....	19
1. Phase decomposition .....	6	C. Electrical and thermal properties .....	21
2. Formation of an fcc-structured $M_{n+1}(A,X_n)$ phase .....	7	VI. SUMMARY AND FUTURE PERSPECTIVES .....	21
		A. Systematic, application-oriented research design ..	21

B. Expanded compositional space .....	22
C. MAX phase thin films and composites .....	23
D. MAX-derivative phases .....	23
E. MAB phases .....	25

## I. INTRODUCTION

The  $M_{n+1}AX_n$  (commonly referred to as MAX) phases are a group of hexagonal compounds, where M represents an early transition metal, A is an A group (mostly III A and IV A group) element, X is carbon and/or nitrogen, and  $n = 1, 2$ , or  $3$ . The MAX phases were first synthesized by Nowotny and colleagues in the 1960s, who referred to them at the time as “H-phases.”<sup>1–5</sup> However, they attracted little interest prior to the mid-1990s when Barsoum and his colleagues successfully synthesized a single-phase, bulk, dense  $Ti_3SiC_2$  sample.<sup>6</sup> In 2000, Barsoum published the first detailed review of these compounds, labeling them as  $M_{n+1}AX_n$  phases. These materials can be described as thermodynamically stable nanolaminates—M-X layers sandwiched between A layers—and, due to these unusual structures, exhibit unique combinations of properties typical of both metals and ceramics.<sup>7</sup> These properties include high electrical and thermal conductivity, exceptional resistance to oxidation and corrosion, easy machinability, low density, high elastic stiffness, and excellent damage tolerance, to name a few.<sup>8–15</sup> These remarkable combinations of properties make MAX phases attractive for a variety of technological applications, particularly relative to other refractory binary transition-metal carbides and nitrides, which often exhibit poor machinability, intrinsic brittleness, and poor oxidation resistance.<sup>16</sup> MAX phases have often been proposed for high-temperature applications, such as high-temperature foil bearings,<sup>17</sup> heating elements,<sup>18</sup> and electrical contacts.<sup>19</sup> In addition to their tolerance for high-temperature conditions, many MAX phases are highly resistant to radiation damage; they are considered promising candidate materials for current nuclear reactors (e.g., as coatings on zirconium alloy fuel cladding in Gen-II/III light water reactors)<sup>20,21</sup> and for advanced nuclear systems (e.g., coatings or structural materials in Gen-IV reactors and structural components in fusion reactors).<sup>22–26</sup>

In nuclear reactors, materials commonly experience high temperatures, chemically reactive environments, and intense radiation fields that can lead to severe degradation of their physical and mechanical properties. Irradiation, wherein materials are bombarded with energetic particles, leads to the production of large quantities of defects, such as Frenkel defect pairs. At high radiation fluences, the accumulation of many point defects can cause the formation of extended defects, including dislocation loops, stacking faults, and voids. Over larger length-scales, defect production can alter the structures of materials by phase transformation or amorphization, deleteriously influencing their properties via processes such as radiation-induced hardening, solute segregation, irradiation creep, void swelling, and helium embrittlement.<sup>27,28</sup>

While the development of radiation tolerant materials has long been pursued in the nuclear industry, the 2011 Fukushima Daiichi accident—the most severe nuclear accident since the 1986 Chernobyl disaster—catalyzed a search for novel materials that might improve nuclear reactor safety, performance, and efficiency.<sup>29</sup> In particular, considerable research has been devoted to the design and development of accident tolerant fuel (ATF), referring to nuclear fuel assemblies

that are less susceptible to the Zr-based fuel cladding failure due to reaction with coolant water that occurred in Fukushima.<sup>30–32</sup> MAX phases are considered as potential coating materials on ATF cladding to protect the zirconium alloy (Zircaloy) tubes through the formation of a thin cohesive and adhesive alumina or titania layer on the surface.<sup>21,32,33</sup> Because any fuel assembly material will be exposed to extensive irradiation during reactor operation, understanding the responses of coating and structural materials, like the MAX phases, to neutron and ion irradiation is critical to improving nuclear reactor safety and performance.

To date, roughly 155 MAX phases have been discovered.<sup>34</sup> This chemical diversity provides tremendous potential for tuning the properties of these materials to optimize their performance for nuclear applications. In this paper, we review recent advances in the experimental and theoretical study of MAX phase behavior in extreme environments. Emphasis is placed on the mechanisms of structural evolution induced by irradiation and the role of various structural factors in the radiation tolerance of MAX phases. Elucidation of the physical characteristics governing the radiation response of these materials provides a means of designing new materials with better performance under extreme conditions. Additionally, because property degradation is of primary interest from an engineering perspective, this review discusses the available research on radiation-induced property evolution, and we identify gaps in the current understanding of these effects.

## II. STRUCTURES AND PROPERTIES OF UNIRRADIATED MAX PHASES

### A. Structure

The MAX phases exhibit highly ordered hexagonal (hex) nanolayered structures ( $P6_3/mmc$ ) that can be described as  $n$  layers of edge-sharing  $M_6X$  octahedra interleaved by close-packed A-layers. The octahedra are similar to those of the corresponding binary MX compounds (with rock salt structures) and are arranged in a twinned orientation with the A layers as mirror planes. The X atoms are located at the octahedral interstitial sites between the M layers. Based on the  $n$  value, the common MAX phases can typically be categorized, based on stoichiometry, as 211 phases for  $M_2AX$  ( $n = 1$ ), 312 phases for  $M_3AX_2$  ( $n = 2$ ), and 413 phases for  $M_4AX_3$  ( $n = 3$ ), as shown in Fig. 1(a). These 211, 312, and 413 phases are distinguished primarily by the number of M layers between the A layers. Table I summarizes unit cell parameters and detailed structural information of three representative MAX phases:  $Ti_2AlC$ ,  $Ti_3AlC_2$ , and  $Ti_4AlN_3$ .

$M_{n+1}AX_n$  phases exhibit one of three distinct stacking sequences, referred to as  $\alpha$ -,  $\beta$ -, and  $\gamma$ -types. As shown in Fig. 1(a), the  $\alpha$ -type stacking sequence along the [0001] direction of  $M_{n+1}AX_n$  phases is as follows:



where the greek letters refer to the X layers, the underlined letters to A layers, and the remaining letters to M layers.  $\beta$ - and  $\gamma$ -type structures, which exist for the 312 and 413 phases (e.g.,  $\beta$ - $M_3AX_2$ ,<sup>38</sup>  $\beta$ - $M_4AX_3$ ,<sup>39</sup> and  $\gamma$ - $M_4AX_3$ <sup>40</sup>), have slightly different atomic arrangements. Figure 1(b) shows schematically the structure of a representative 312 phase,  $\alpha$ -type  $Ti_3AlC_2$ , along [11 $\bar{2}$ 0], where the twinning structure of the MX slabs (i.e., the zig-zag stacking sequence) is apparent. Because this

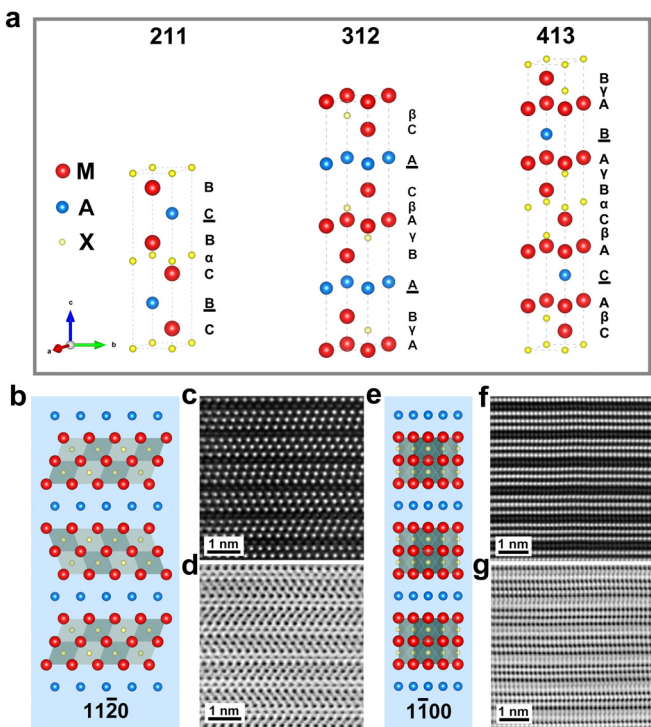


**FIG. 1.** (a) Unit cells of 211, 312, and 413 MAX phases. The stacking sequences of all atoms are shown to the right of each unit cell. The atomic arrangement of a representative 312 MAX phase,  $Ti_3AlC_2$ , is shown along (b)  $[1\bar{1}20]$  and (e)  $[1100]$ , as well as the corresponding [(c) and (f)] STEM HAADF images and [(d) and (g)] ABF images. Note that the intensity of each atomic column is element dependent.

stacking sequence comprehensively describes the structure of these compounds, it is most important to characterize the structure along  $[1\bar{1}20]$  in studies of MAX phase structures.

Due to the separated layered structure, an advanced imaging technique, aberration-corrected scanning transmission electron microscopy (STEM), is commonly used to directly characterize different elemental layers at the atomic scale.<sup>41–47</sup> The intensity of an atomic column in high-angle annular dark-field (HAADF) STEM images is proportional to  $\sim Z^2$  ( $Z$  represents the atomic number), such that

HAADF allows for accurate chemical differentiation of relatively heavy elements.<sup>48</sup> Therefore, M and A layers can be readily distinguished in the HAADF images, as shown in Fig. 1(c), where Ti layers exhibit a brighter contrast compared with Al layers.

More recently, another STEM technique, annular bright-field (ABF) imaging, has enabled direct observation of light elements in these materials. The intensity of atoms in annular bright-field (ABF) STEM images follows a  $Z^{1/3}$  dependency, making ABF more sensitive to relatively light elements.<sup>49</sup> We recently, for the first time, employed this technique to observe C atoms in  $Ti_3AlC_2$  before and after ion irradiation.<sup>47</sup> Figure 1(d) shows that the C atoms are located at the octahedral interstitial sites between the Ti layers, providing the first direct imaging evidence of the anion positions in MAX phases. In combination, STEM HAADF and ABF imaging techniques serve as powerful, complementary methods for characterizing the structural evolution of  $M_{n+1}AX_n$  phases.

To enhance the accuracy of the structural analysis of the MAX phases, some researchers have imaged the materials along  $[1\bar{1}00]$  at an angle of  $30^\circ$  with  $[11\bar{2}0]$ .<sup>50–52</sup> Figures 1(e)–1(g) show the structural model in this direction, as well as corresponding STEM HAADF and ABF images of  $Ti_3AlC_2$ . Compared with the images along  $[11\bar{2}0]$ , the zig-zag stacking sequence cannot be observed along  $[1\bar{1}00]$ . However, the images corroborate the ordered distribution of the M/A atoms and the arrangement of the X atoms.

Besides the common  $M_{n+1}AX_n$  phases ( $n = 1, 2, 3$ ) mentioned above, researchers have also described the existence of other MAX and derivative phases. These include the following:

- (1) higher order  $M_{n+1}AX_n$  phases ( $n = 4, 5, 6$ ), such as 514, 615, 716 phases<sup>52–54</sup>
- (2) ordered  $(M, M')_{n+1}AX_n$  phases, such as  $Cr_2TiAlC_2$ <sup>51</sup> and  $Mo_2Ti_2AlC_3$ <sup>55</sup>
- (3) random solid solution phases, such as  $Ti_3(Al_{1-x}Si_x)C_2$ <sup>56</sup> and  $Ti_2Al(C_xN_y)$ <sup>57</sup>
- (4) hybrid MAX phases, such as  $M_5A_2X_3$  and  $M_7A_2X_5$ <sup>53</sup>
- (5) other derivative phases, such as  $(MC)_n(Al_3C_2)_m$  and  $(MC)_n(Al_4C_3)_m$ .<sup>58,59</sup>

## B. Key thermal, mechanical, and chemical properties

To fulfill the requirements for structural materials in nuclear energy systems, three aspects of MAX phases are most important: thermal properties, mechanical properties, and chemical reactivity (i.e., corrosion and oxidation).

**TABLE I.** Unit cell parameters and structural information of  $Ti_2AlC$ ,  $Ti_3AlC_2$ , and  $Ti_4AlN_3$ .

Formula	$Ti_2AlC$ <sup>35</sup>		$Ti_3AlC_2$ <sup>36</sup>		$Ti_4AlN_3$ <sup>37</sup>	
Unit cell parameters ( $\text{\AA}$ )	$a = 3.06$		$a = 3.08$		$a = 2.99$	
	$c = 13.60$		$c = 18.58$		$c = 23.37$	
Structural information	Wyckoff notation	Atomic positions	Wyckoff notation	Atomic positions	Wyckoff notation	Atomic positions
	Ti (4f)	(1/3, 2/3, 0.064)	Ti(I) (2a)	(0, 0, 0)	Ti(I) (4f)	(1/3, 2/3, 0.054)
	Al (2d)	(1/3, 2/3, 3/4)	Ti(II) (4f)	(2/3, 1/3, 0.128)	Ti(II) (4e)	(0, 0, 0.155)
	C (2a)	(0, 0, 0)	Al (2b)	(0, 0, 1/4)	Al (2c)	(1/3, 2/3, 1/4)
	...	...	C (4f)	(1/3, 2/3, 0.064)	N(I) (2a)	(0, 0, 0)
	...	...	...	...	N(II) (4f)	(2/3, 1/3, 0.105)

### 1. Thermal properties

Due to their refractory nature and high melting points, some MAX phases are attractive candidate materials for high-temperature applications. Most ceramics exhibit brittleness and are susceptible to thermal shock damage.<sup>60,61</sup> In contrast, the response of MAX phases to thermal shock differs from that of other ceramics, which may be attributed to the formation of compressive stresses on the surface oxide layer,<sup>62</sup> the substantial metallic character of the bonding, and the formation of kink bands in the substrate.<sup>63</sup> As a result, certain MAX phases, such as  $Ti_3AlC_2$  and  $Ti_3SiC_2$ , show excellent shock resistance, high damage tolerance, and good ductility.<sup>64,65</sup> Additionally, the thermal conductivity of most MAX phases ranges from roughly 26 to 60 W/m-K (for example, 46 W/m-K for  $Ti_2AlC$ ) at ambient temperature and greater than 20 W/m-K at high temperatures (800 K) for some compositions.<sup>12</sup> These are higher than most ceramics and even some metals or alloys, such as pure Ti and Zircaloy.<sup>66</sup> This conductivity ensures that the thermal energy generated in nuclear energy components, such as nuclear fuel assemblies in fission reactors, can be efficiently transferred through Zircaloy and MAX phase coatings to the reactor coolant (i.e., water, gas, and molten salt).

### 2. Mechanical properties

The MAX phases are relatively soft, with a hardness ranging from 2 to 8 GPa. This can be explained by their easy basal plane slip due to the layered structure and the relatively weak coupling between MX slabs and A layers.<sup>11</sup> These characteristics make the MAX phases easily machinable, which is one of their most attractive properties, as compared with conventional ceramics, in terms of industrial use. Despite their softness, these materials are elastically stiff with high fracture toughness and low densities.<sup>67</sup> In addition, some MAX phases are damage tolerant at room temperature and deform plastically as temperature increases.<sup>68</sup> Data on the fatigue and creep behavior of MAX phases are limited, with mainly  $Ti_3SiC_2$  studied.  $Ti_3SiC_2$  exhibits higher fatigue resistance than conventional structural ceramics, which is attributed to its heterogeneous and layered structure.<sup>69</sup>

The phase stability of MAX phases under extreme thermomechanical environments (high temperature and mechanical stresses) also plays an important role in their application in nuclear systems. Heating by nuclear fission and radioactive decay set stringent temperature requirements for in-core structural materials in current GEN-II and GEN-III reactors, around  $\sim 300$ – $400$  °C; those of the six proposed GEN-IV reactors range from 300 to 1000 °C, depending on type.<sup>27</sup> At temperatures below 1000 °C, most MAX phases are structurally stable, except, for example,  $Cr_2GaN$  that decomposes at  $\sim 850$  °C.<sup>70</sup> In vacuum, the phase decomposition temperatures for some representative bulk MAX phases samples,  $Ti_2AlC$ ,  $Ti_3AlC_2$ , and  $Ti_3SiC_2$ , range from 1500 to 2200 °C.<sup>71–73</sup> Phase decomposition is caused by the out-diffusion of A away from the unit cell, eventually leading to the formation of binary  $M_{n+1}X_n$  via the relaxation of remaining twinned MX slabs and X rearrangement.<sup>72</sup> In practice, the precise decomposition temperature is also influenced by the presence of impurities and the chemical environment.<sup>74</sup>

In nuclear reactors, irradiation-induced fuel swelling and cladding failure can cause mechanical stresses on MAX phase coatings, in addition to the high-temperature conditions. The high pressure that such stresses produce at some localized areas, such as crack tips, can

be much higher than those applied to the fuel pellets (MPa). Interestingly, most MAX phases are remarkably stable under high pressure (hydrostatic) up to tens of GPa.<sup>75–77</sup> Only a few undergo substantial phase modification, such as  $\alpha$ - $Ti_3GeC_2$ , which transforms to the similarly-structured  $\beta$  phase in response to large shear stresses (non-hydrostatic).<sup>78</sup>

### 3. Chemical stabilities

Alongside these critical thermal and mechanical properties, the resilience of MAX phases in harsh chemical environments is an important benefit for their use in nuclear energy systems. In reactors, coolant is used to transfer heat/energy from the reactor core to turbines for the generation of electricity. Direct contact of coolant with structural materials, for example, potential MAX phase coatings on nuclear fuel elements, can result in corrosion of these materials at high temperatures. The coolant in most currently operating reactors is water, sometimes including deuterium oxide.

Al-based MAX phases show excellent corrosion and oxidation resistance in water and air.<sup>79,80</sup> The mechanism can be briefly explained by the formation of a dense, continuous  $Al_2O_3$  layer that protects the MAX phase substrate. Recently, researchers have studied the corrosion behavior of the MAX phases in molten metals (Na, Pb, Pb-Bi) and molten salt (FLiNaK, less chemically reactive than Na), both of which serve as coolants in GEN-IV reactors [e.g., sodium-cooled fast reactors (SFR) and molten salt reactors (MSR)].  $Ti_2AlC$ ,  $Cr_2AlC$ , and  $Ti_3SiC_2$  do not react with Na at 750 °C,<sup>81</sup> while  $Ti_3SiC_2$  is quite stable in molten Pb and Pb-Bi alloys.<sup>26</sup> Some compositional trends in corrosion resistance have also been demonstrated. For example,  $Ti_3SiC_2$  has been shown to exhibit superior corrosion resistance in FLiNaK salt than  $Ti_3AlC_2$ , based on its lower mass loss following exposure.<sup>82</sup>

Additional information about the structures and properties of MAX phases can be found elsewhere.<sup>9,11–13,34,46,67,83</sup>

### III. RADIATION-INDUCED STRUCTURAL EVOLUTION IN MAX PHASES

While the MAX phases were first considered as candidate materials for high-temperature applications decades ago, their response to irradiation was not studied until around 2009.<sup>84</sup> Structural materials in nuclear reactors are exposed to a complex and extreme environment, wherein irradiation by both neutrons and various fission fragments (such as, He from alpha-decay and accelerated Kr, Zr, Ba and Xe ions) can change the structure and properties of these materials. Ion irradiation is commonly used to simulate the irradiation conditions in nuclear reactors in isolation with lower cost and time requirements.<sup>85</sup> However, the production of radiation damage strongly depends on the ion mass and energy due to the associated variation in electronic energy loss, energy spectrum of primary knock-on atom, and chemical alteration accompanying ion implantation.<sup>86</sup> Therefore, considering the chemical diversity of the MAX phases, and the possible irradiation conditions, some key questions remain unresolved. First, the mechanisms of the structural evolution induced by irradiation have been debated for many years.

As an energetic ion or neutron traverses a material, it can cause defect production and damage in the periodic atomic structure. To evaluate the damage level induced by particle (low energy) bombardment in nuclear materials, displacement per atom (dpa) is used as the current international standard for approximate quantification, which can be calculated by SRIM software,<sup>87</sup> among types of models.<sup>88</sup> As

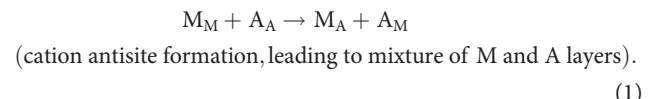
the ion energy increases to approximately 1 MeV/u or greater, ions deposit the majority of their energy in materials via electronic energy loss, leading to structural modifications in ceramics, including formation of defects, phase transformation, decomposition, and amorphization.

### A. Formation of M/A antisite defects

In MAX phases, there exist various kinds of defects, including point defects, stacking faults, and dislocations that are formed under different extreme environments.<sup>89</sup> At the early stage of irradiation (low particle fluence), defects usually exist in the form of isolated point defects, such as interstitials, vacancies, Frenkel pairs, and antisite defects (e.g., M atoms are displaced to sites initially occupied by A atoms, and *vice versa*) in MAX phases. As the fluence increases, clustering of defects becomes more likely. Le Flem *et al.*<sup>23</sup> observed black dots in TEM imaging of the  $Ti_3(Si, Al)C_2$  thin film sample after irradiation by 92 MeV Xe ions, as indicated by the white arrows in Fig. 2(a). These black dots correspond to clusters of these point defects or other local structure changes. In previous studies, first-principles calculations were employed to investigate various types of defects, including their formation energy. This work clearly shows that, for all MAX phases, antisite defects in all the MAX studied possess the lowest formation energies among all defect types, indicating that their formation is more energetically favorable.<sup>90–93</sup> For example, the formation energy of the  $Al_{Ti}$  antisite defect in  $Ti_3AlC_2$  is 0.74 eV, as compared with 1.32 eV and up for other defect types.<sup>91</sup>

More recently, we, for the first time, directly imaged the formation of antisite defect clusters in  $Ti_3AlC_2$  induced by Au ion irradiation,<sup>47</sup> as shown in Fig. 2(b). Irradiation induces slight structural modification in  $Ti_3AlC_2$  at a relatively low ion fluence ( $\sim 0.2$  dpa), while the hexagonal structure is retained. As mentioned above, the STEM HAADF imaging technique allows direct atom-by-atom imaging and chemical identification for heavy elements, i.e., M and A cations in the MAX phases, based on the intensity/contrast of atomic

columns in the image. Compared with the initial structure shown in Fig. 1(c), the intensities of some Al columns increase after irradiation, as indicated by the white arrows in Fig. 2(b), while those of some adjacent Ti atoms are attenuated. This intensity variation is also shown in the intensity profile along the Al layer (line 2) and the Al-Ti-Ti-Ti-Al layers (line 1), as shown in Figs. 2(c) and 2(d). This indicates the formation of clusters of  $Ti_{Al}-Al_{Ti}$  antisite defects, leading to a chemical disordering process at the M/A cation sites that can be described as



Similar irradiation-induced chemical order-to-disorder transformations have been widely observed in complex oxides, such as the  $Ln_2B_2O_7$  compounds that are used for the immobilization of actinide nuclear wastes.<sup>94–96</sup> In these materials, irradiation drives phase transformations from initially ordered pyrochlore structures to chemically disordered, face-centered cubic (fcc)-structured  $(Ln_2B_2)O_7$  solid solutions by the formation of  $Ln_B-B_{Ln}$  antisite defects at the cation sites. This disordering process strongly influences materials' properties, including the thermal and mechanical properties important for material performance in nuclear reactors.<sup>97</sup> Therefore, understanding the mechanisms of these order-to-disorder transformations in the MAX phases is critical to their technological application.

### B. Structural evolution

In nearly all MAX phases, room temperature irradiation induces the formation of new phases with an fcc-like structure. This transformation typically begins at a specific threshold fluence value, depending on the irradiation conditions (i.e., ion or neutron, ion energy, and ion type).<sup>47,98–110</sup> Figure 3 illustrates x-ray diffraction (XRD) evidence of the structural evolution in eight representative MAX phases. Only the  $Cr_2AlC$  becomes amorphous without forming the new fcc phase, as

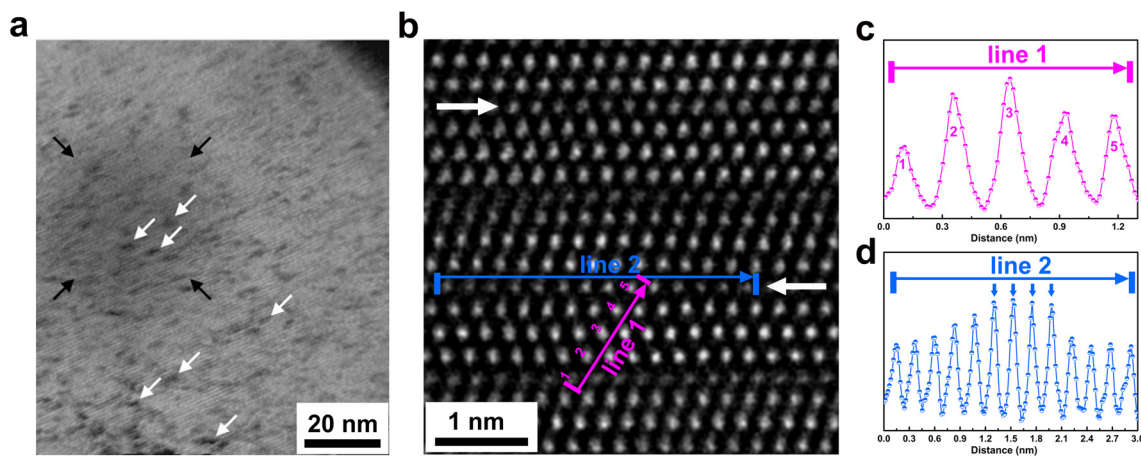


**FIG. 2.** (a) A TEM image of  $Ti_3(Si, Al)C_2$  irradiated to 0.2 dpa (92 MeV Xe ion,  $1 \times 10^{15} \text{ cm}^{-2}$ ). The white arrow indicates a cluster of point defects (black dots). Reproduced with permission from Le Flem *et al.*, Int. J. Appl. Ceram. Technol. 7(6), 766–775 (2010). Copyright 2010 The American Ceramic Society. (b) STEM HAADF image of  $Ti_3AlC_2$  irradiated with 1 MeV Au ions to a fluence of  $1 \times 10^{15} \text{ cm}^{-2}$ , imaged along  $[11\bar{2}0]$ , showing direct evidence of cation antisite defects. The white arrows indicate the initial Al layers, whose image contrast is altered compared with the initial hexagonal structure. [(c) and (d)] Contrast profiles along line 1 and 2 in (b), respectively, which directly show the variation of contrast arising from the formation of  $Ti_{Al}-Al_{Ti}$  antisite defects produced by ion irradiation.

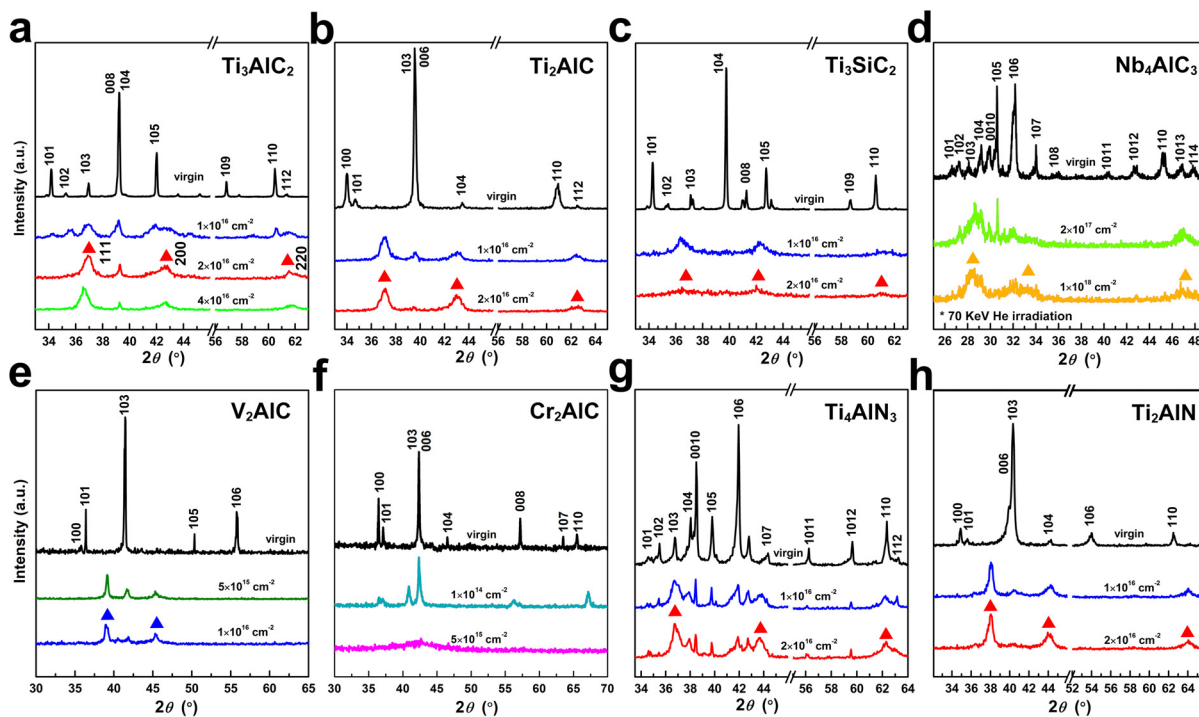


**FIG. 3.** Grazing incidence X-ray diffraction (GIXRD) patterns of (a)  $\text{Ti}_3\text{AlC}_2$ , (b)  $\text{Ti}_2\text{AlC}$ , (c)  $\text{Ti}_3\text{SiC}_2$ , (d)  $\text{Nb}_4\text{AlC}_3$ , (e)  $\text{V}_2\text{AlC}$ , (f)  $\text{Cr}_2\text{AlC}$ , (g)  $\text{Ti}_4\text{AlN}_3$ , and (h)  $\text{Ti}_2\text{AlN}$ .  $\text{Nb}_4\text{AlC}_3$  was irradiated with 70 KeV He ions, while the rest were irradiated with 1 MeV Au ions. In all compounds except  $\text{Cr}_2\text{AlC}$ , ion irradiation drives the formation of new fcc structures, whose diffraction peaks are indicated by triangles. The threshold fluence for the onset of the observed phase transformation differs among the materials, indicating different susceptibilities to irradiation induced damage. Reproduced with permission from Wang *et al.*, J. Am. Ceram. Soc. **99**(5), 1769–1777 (2016). Copyright 2016 The American Ceramic Society.

16 April 2024 01:28:24

shown in Fig. 3(f), which will be discussed later. The precise mechanisms of this structural evolution, resulting from exposure of these materials to radiation, have been studied and debated for many years.<sup>47,98,107,111,112</sup> Explanations proffered to date for the formation of the fcc-structured phases fall into three main categories: phase decomposition to binary MX, disordering to a solid solution  $\text{M}_{n+1}(\text{A},\text{X}_n)$  phase, or disordering to a  $(\text{M}_{n+1},\text{A})\text{X}_n$  solid solution phase.

### 1. Phase decomposition

Initially, several researchers argued that irradiation triggers phase decomposition from ternary compounds into the corresponding binary fcc-structured carbides or nitrides, accompanied by out-diffusion of A elements.<sup>98–101,112,113</sup> This reasoning was based on the observation that some MAX phases are not stable under specific extreme environments, such as high temperatures,<sup>10,114</sup> oxygen-enriched environments,<sup>115</sup> hydrothermal environments,<sup>116</sup> and acidic/alkaline environments,<sup>117,118</sup> and that these conditions, ostensibly analogous to those of irradiation, induce phase decomposition processes.

The tendency of MAX phases to decompose under extreme environments is explained by their defect energetics. Zhang *et al.*<sup>119</sup> reported that the migration energy barriers of  $\text{V}_{\text{Si}}$ ,  $\text{Si}_\beta$ , and  $\text{Ti}_{\text{Si}}$  along the Si atomic plane in  $\text{Ti}_3\text{SiC}_2$  are only 0.9, 0.6, and 0.3 eV, respectively. Additionally, the M-A bond is typically the weakest among all

bonds, and the M-A bond distance is typically the longest in MAX phases. This makes the migration of atoms along the A layers, as is necessary for A out-diffusion at grain boundaries and surfaces, relatively easy.

For example,  $\text{Ti}_3\text{AlC}_2$  remains stable up to around 1300 °C, after which it decomposes due to Al out-diffusion as shown in Fig. 4, via the reaction<sup>10</sup>



After A out-diffusion, the initial A positions/layers can be occupied by other atoms (i.e., Au, Cu, Ir) or functional groups (i.e., O, F, OH). In fact, phase decomposition has been utilized to synthesize new materials, such as noble-metal-containing transition-metal carbides/nitrides<sup>120</sup> and two-dimensional MXene nanosheets.<sup>117,118</sup> As the  $\text{MX}_{n/\text{n}+1}$  layers that remain after A out-diffusion are annealed at relatively high temperature, the X anions initially located between the M layers migrate to partially-empty A layers, as shown in Fig. 4(c). The remaining twinned  $\text{M}_{n+1}\text{X}_n$  slabs can be detwinned and recrystallize to (111)-oriented  $\text{MX}_{n/\text{n}+1}$  layers, accompanied by the formation of voids in the material,<sup>114</sup> as shown in Fig. 4(d).

Based on these studies, interpretation of the irradiation-induced transformation as a phase decomposition process appears reasonable. However, many MAX phases show no evidence of irradiation-induced formation of voids that should accompany a phase decomposition process. One exception is in  $\text{Ti}_3\text{AlC}_2$  under 200 keV electron

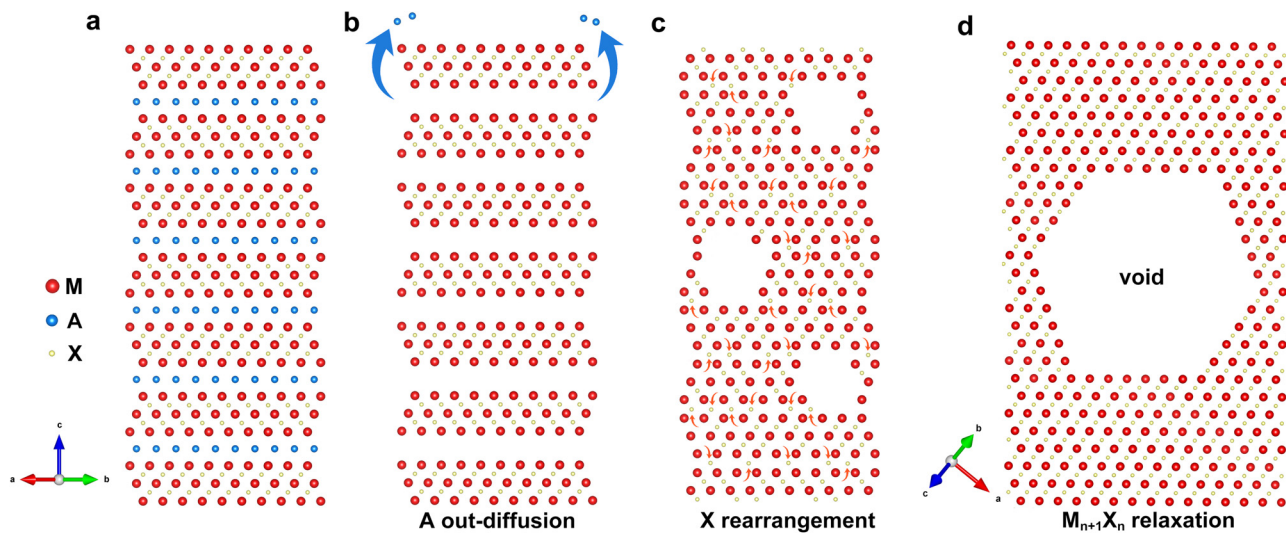


**FIG. 4.** Schematic illustration of different stages of phase decomposition in MAX phases. (a) Initial hexagonal structure. (b) A out-diffusion and evaporation. (c) X rearrangement with void formation. (d) MX relaxation, de-twinning, and void growth. Reproduced with permission from Emmerlich *et al.*, *Acta Mater.* **55**, 1479–1488 (2007). Copyright 2006 Acta Materialia, Inc., published by Elsevier Ltd.

irradiation. After exposure to an electron beam for 500 s, it was found that Al atoms were sputtered away with no evidence of amorphization.<sup>121</sup> However, in other studies of MAX phases, these materials were found to be stable under electron beam irradiation, even at higher voltage. Additionally, few studies show phase instability of the MAX phases under irradiation. Tunes *et al.* investigated the structural response of MAX phases to neutron irradiation, up to 10 dpa at 1000 °C.<sup>122</sup> Their results show that needlelike precipitates formed in Ti<sub>2</sub>AlC after irradiation, indicating the possibility of phase decomposition. Although this evidence shows that precipitates are formed in some grains (not all), the stability of these compounds under irradiation still requires further investigation. The limited observation of phase decomposition might be due to the quality of the sample or other issues extrinsic to the MAX phases.

## 2. Formation of an fcc-structured $M_{n+1}(A,X_n)$ phase

Bugnet *et al.*<sup>123</sup> studied the effects of antisite defect formation in irradiated Ti<sub>3</sub>AlC<sub>2</sub> using *ab initio* calculations and electron energy loss spectroscopy/x-ray absorption spectroscopy (EELS/XAS) and proposed a new structural model for the fcc phase. In their model, irradiation leads to the substitution of Al atoms on C sites and triggers phase transformation to a newly formed fcc-structured Ti(Al<sub>0.33</sub>C<sub>0.67</sub>) phase at a dose of 2 dpa. They argued that the new phase was different from the  $\alpha$ -Ti<sub>3</sub>AlC<sub>2</sub> and  $\beta$ -Ti<sub>3</sub>AlC<sub>2</sub> phases and possesses a structure based on that of the related material, TiC, as evidenced by the similarity of their d-spacings along [111].

Through analysis of the C-K and Al-K edges of initial and irradiated samples, they studied the local order in the Ti<sub>6</sub>C octahedral layers and the detailed charge distribution around Al atoms. These results show that the Al atoms were displaced from a highly anisotropic trigonal prismatic site to a more isotropic atomic site. The simulated C-K energy loss near edge structure (ELNES) of the proposed

Ti(Al<sub>0.33</sub>C<sub>0.67</sub>) structure is in good agreement with the experimental results.

The structure of the proposed Ti(Al<sub>0.33</sub>C<sub>0.67</sub>) phase differs from that of TiC in the presence of Al atoms (occupancy 0.33) at the anion sites. The structure seems reasonable because both the cation and anion sites are fully occupied and *ab initio* calculations show that it remains after relaxation. However, in the absence of direct observation of the structure of the irradiated sample, the proposed structure might be inaccurate. First, in previous studies, Ti<sub>3</sub>AlC<sub>2</sub> exhibits a high degree of radiation tolerance and retains its hexagonal structure at a low damage level ( $\sim 2$  dpa).<sup>24,124</sup> Therefore, the formation of fcc phase is unlikely under these conditions. In addition, Yang *et al.*<sup>102</sup> recently found that irradiation drives a phase transformation to a hexagonal metastable phase before the formation of an fcc phase. This metastable phase is a new  $\gamma$  phase, whose d-spacing along [1100] is similar to the results shown in Bugnet's study. Therefore, it is believed that the phase formed in Bugnet's study is the hexagonal  $\gamma$  phase, rather than an fcc-structured phase.

Regardless of the accuracy of their structural model, Bugnet *et al.* provided detailed information on Ti/Al and Al/C antisite defects and developed a new and important approach (a combination of EELS/XAS and *ab initio* calculations) for probing the local structure of disordered MAX phases.

## 3. Formation of an fcc-structured $(M_{n+1},A)X_n$ phase

More recently, additional studies have shown that MAX phases undergo a multi-step transformation process from hexagonal  $\alpha$  to  $\beta$  to  $\gamma$  to the fcc phase. As mentioned above, A atoms can readily migrate along the A layers. For example, the Si atoms in  $\alpha$ -Ti<sub>3</sub>SiC<sub>2</sub> can move from the initial 2b sites to 2d sites, driving the formation of the  $\beta$ -Ti<sub>3</sub>SiC<sub>2</sub> phase. The stacking sequence of the  $\beta$ -Ti<sub>3</sub>SiC<sub>2</sub> phase is  $\beta$ CBC $\beta$ A $\gamma$ BCB $\gamma$ A, as shown in Fig. 5(b). Liu *et al.*<sup>24</sup> found that  $\alpha$ -Ti<sub>3</sub>Si<sub>0.9</sub>Al<sub>0.1</sub>C<sub>2</sub> partially transforms into  $\beta$ -Ti<sub>3</sub>Si<sub>0.9</sub>Al<sub>0.1</sub>C<sub>2</sub> when

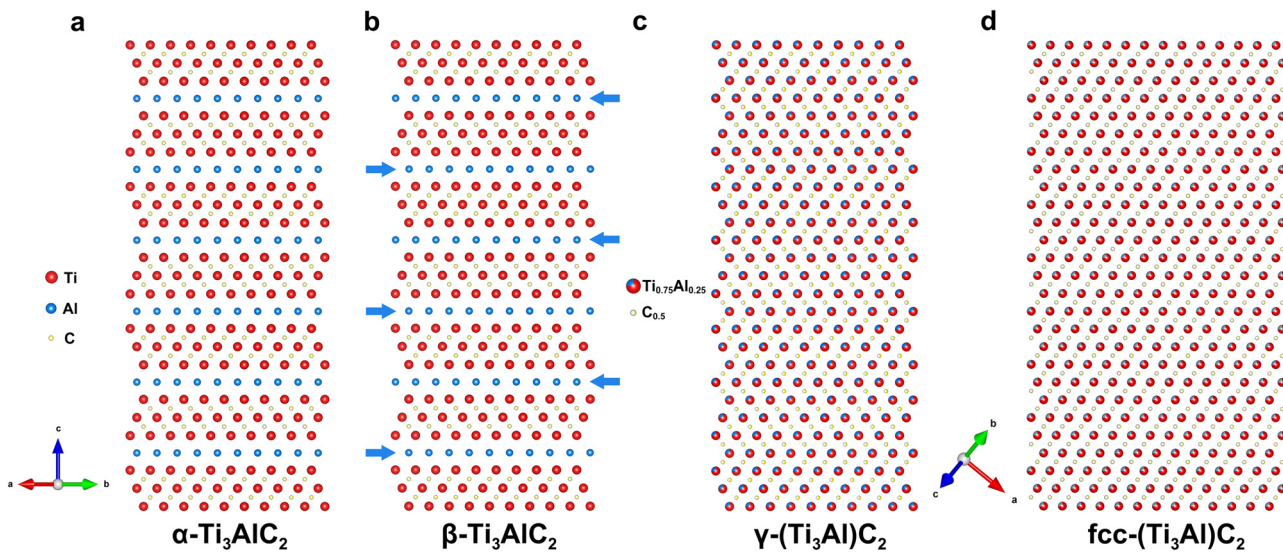


**FIG. 5.** Schematic illustration of different stages of phase transformation in  $\text{Ti}_3\text{AlC}_2$ . (a) Initial hexagonal structure. (b)  $\beta\text{-Ti}_3\text{AlC}_2$  in which the blue arrows indicate different positions of the Al atoms compared with the initial  $\alpha\text{-Ti}_3\text{AlC}_2$  phase. (c)  $\gamma\text{-(Ti}_3\text{Al)}\text{C}_2$  solid solution, in which the Ti and Al atoms are uniformly distributed at the cation sites and C atoms are distributed at the anion sites due to the accumulation of Ti/Al antisite defects and C rearrangement. (d)  $\text{fcc-(Ti}_3\text{Al)}\text{C}_2$  solid solution, which indicates phase transformation due to the formation of stacking faults.

irradiated with 92 MeV Xe ions, based on Rietveld refinement of XRD patterns. The amount of the  $\beta\text{-Ti}_3\text{Si}_{0.9}\text{Al}_{0.1}\text{C}_2$  phase increased with further irradiation due to the increase in the number of interstitials. Similar phase transformations from the  $\alpha$  phase to  $\beta$  phase were also observed in  $\text{Ti}_3\text{AlC}_2$  irradiated with 1 MeV  $\text{C}^{4+}$  ions at various temperatures.<sup>110</sup> This phase transformation process and further atomic migration along the A layers could help to accommodate a large number of structural defects, which are induced by extreme environments without any major alteration of the structure.

On the other hand, antisite defects have been observed in the early stage of irradiation, as shown in Fig. 2(b). As further irradiation generates additional antisite defects, the disordering occurs at both the cation and anion sites. The accumulation of such defects eventually leads to the formation of a hexagonal  $\gamma$  phase, which has been observed in irradiated  $\text{Ti}_3\text{AlC}_2$ ,<sup>110</sup>  $\text{Ti}_2\text{AlC}$ ,<sup>104</sup>  $\text{Ti}_4\text{AlN}_3$ ,<sup>106</sup>  $\text{Ti}_2\text{AlN}$ ,<sup>108</sup>  $\text{V}_2\text{AlC}$ , and  $\text{Cr}_2\text{AlC}$ ,<sup>105</sup> as shown in Fig. 5(c). Compared with HAADF images of the pristine sample [Figs. 1(c) and 1(f)], in which the M and A atomic columns show an apparent contrast difference, the HAADF image of the  $\gamma$  phase shows identical contrast in each atomic column, as shown in Figs. 6(c) and 6(f). This indicates that the M and A atoms are uniformly distributed at the cation sites with the occupancy ratio of  $n+1/1$  in the  $\gamma$  phase. Meanwhile, ABF images [Figs. 6(d) and 6(g)] show that, along with mixing of occupancy at the cation sites, the X atoms that were initially located between the M layers move, eventually occupying the octahedral sites between the rearranged cation (M/A) sites with an occupancy of  $n/n+2$ , as shown in the following reaction:



Therefore, the  $\gamma$  phase can be described as a solid solution,  $\gamma\text{-(M}_{n+1}\text{A})\text{X}_n$ . Following this transformation to the  $\gamma$  phase, the atomic stacking sequence along [0001] becomes  $\beta\text{C}_\text{x}\text{B}_\text{x}\text{C}_\text{x}\beta\text{A}_\text{x}\text{B}_\text{x}\text{C}_\text{x}\text{B}_\text{x}\text{A}_\text{x}$ , with

the cations exhibiting the same sequence as in the  $\beta$  phase. These cation and anion rearrangements also yield d-spacings between layers identical to those of the  $\beta$  phase.

Relatively few studies have reported the observation of the  $\beta$  phase, based on XRD results. In contrast,  $\gamma$  phases have been observed in numerous MAX phases after irradiation, and their detailed structures have been analyzed by various analytic methods [XRD, TEM imagery, and TEM selected-area electron diffraction (SAED)]. There are three main reasons for the limited observation of the  $\beta$  phase: discrete radiation process, poor phase stability under irradiation, and simultaneous occurrence of antisite defects and atomic migration along A layers. First, in most studies, structures analysis is performed only at discrete fluence steps, not continuously. The  $\beta$  phase that forms over a relative narrow range of low fluences might therefore not be observed. Second, the  $\gamma$  phase might have a lower energy than the  $\beta$  phase, such that the metastable  $\beta$  phases, if formed, rapidly transform into the  $\gamma$  phase as the fluence increases. More importantly, since both the migration barrier of atoms along the A layers and the formation energy of antisite defects are low, it is likely that both processes occur simultaneously rather than successively (yielding a transformation from  $\alpha$  to  $\gamma$ , rather than from  $\alpha$  to  $\beta$  to  $\gamma$ ). It is possible that the formation of the metastable  $\gamma$  phases, via an energetically inexpensive atomic rearrangement, can enhance the radiation tolerance of these materials, allowing them to incorporate a high concentration of irradiation-induced defects while maintaining crystallinity.

As the irradiation fluence increases to a relatively high level, the stacking sequence is further altered to  $\text{A}_\text{x}\text{B}_\text{x}\text{C}_\text{x}\text{B}_\text{x}\text{A}_\text{x}\text{C}_\text{x}\text{B}_\text{x}\text{A}_\text{x}$ , as shown in Figs. 6(i)–6(k). This indicates the transformation of the  $\gamma\text{-(M}_{n+1}\text{A})\text{X}_n$  phase to a solid solution fcc phase, i.e.,  $\text{fcc-(M}_{n+1}\text{A})\text{X}_n$  phase,<sup>47,105–110</sup> as shown in Figs. 5(d) and 6(h). Similar to the  $\gamma\text{-(M}_{n+1}\text{A})\text{X}_n$  phases, the cation sites are uniformly occupied by M and A atoms, while the anion sites are occupied by the X atoms with an occupancy of  $n/n+2$ .

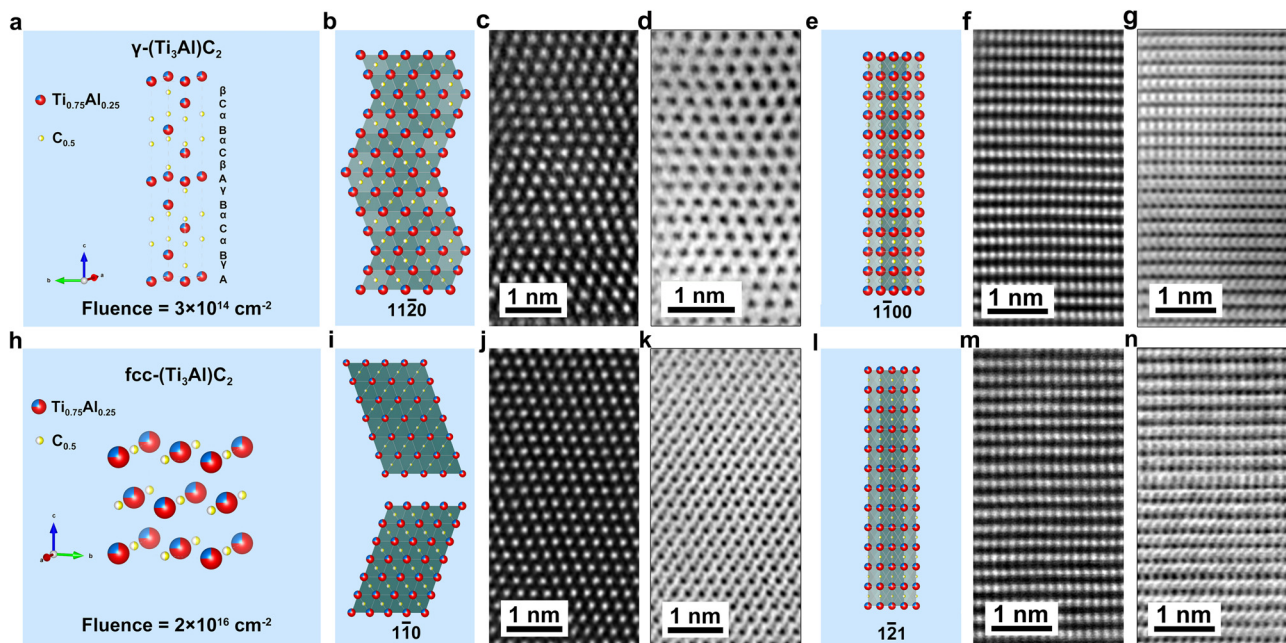


**FIG. 6.** Unit cells, atomic arrangements, STEM HAADF and ABF images along  $[11\bar{2}0]$  and  $[1\bar{1}00]$  of [(a)–(g)]  $\gamma$ - $(\text{Ti}_3\text{Al})\text{C}_2$  and [(h)–(n)] fcc- $(\text{Ti}_3\text{Al})\text{C}_2$ , induced by 1 MeV Au ion irradiation to fluences of  $3 \times 10^{14}$  and  $1 \times 10^{16} \text{ cm}^{-2}$ .

However, the primary difference between the  $\gamma$ - $(\text{M}_{n+1}\text{A})\text{X}_n$  phase and fcc- $(\text{M}_{n+1}\text{A})\text{X}_n$  phase is the stacking sequence. Therefore, the phase transformation from  $\gamma$ - $(\text{M}_{n+1}\text{A})\text{X}_n$  phase to fcc- $(\text{M}_{n+1}\text{A})\text{X}_n$  phase is triggered by the irradiation-induced formation of stacking faults. Generally, in hexagonal MAX phases, stacking faults are generated by the dissociation reactions of perfect dislocations in the basal plane<sup>125</sup> and can be described by

$$\frac{1}{3} \langle 11\bar{2}0 \rangle \rightarrow \frac{1}{3} \langle 10\bar{1}0 \rangle + \text{Stacking Fault} + \frac{1}{3} \langle 01\bar{1}0 \rangle. \quad (4)$$

In most studies, the newly formed fcc- $(\text{M}_{n+1}\text{A})\text{X}_n$  phase exists in a nano-twinned structure<sup>107,111</sup> and persists even as the fluence increases to quite high values (damage levels up to  $\sim 300$  dpa). This ability to maintain the disordered, yet crystalline, fcc phase indicates excellent resistance to irradiation-induced amorphization. Retention of the fcc phase is attributed to the presence of high densities of twin boundaries that strengthen materials<sup>126</sup> and facilitate defect incorporation and annihilation via interstitial emission near grain boundaries.<sup>127</sup>

One exception to this radiation tolerance is found in the Cr based MAX phases. In all studied to date,<sup>105,128,129</sup> phase transformations from the initial phase to the hexagonal  $\gamma$  phase and eventually to an amorphous phase have been observed, with no formation of an fcc phase. This might be attributed to the fact that, unlike TiC, VC, or NbC, the fcc-structured CrC is a metastable phase.<sup>130</sup> Additionally, the structure, bonding, and properties of chromium carbide,  $\text{CrC}_x$ , are strongly dependent on the carbon content,  $x$ .  $\text{CrC}_x$  remains amorphous at low carbon content and crystallinity increases with  $x$ .<sup>131</sup> Analogously, in the  $\gamma$ - $(\text{Cr}_2\text{Al})\text{C}$  phase, the occupancy of carbon is only 0.33, indicating that it is

unlikely to form an fcc- $(\text{Cr}_2\text{Al})\text{C}$  solid solution phase as do the other MAX phases.

All three of the irradiation-induced phase transformation mechanisms discussed above explain the formation of the fcc phase under irradiation, but the precise phase formed differs among them. Recent studies of chemical distribution in irradiated MAX phases show a homogeneous distribution of A in the fcc phase, indicating that out-diffusion did not occur. Atom probe tomography (APT) performed after irradiation of  $\text{Ti}_3\text{AlC}_2$  showed that, in the fcc phase, Al atoms were still uniformly distributed throughout the material, demonstrating a lack of Al out-diffusion.<sup>47</sup> Additionally, XRD characterization of  $\text{Ti}_4\text{AlN}_3$  after irradiation shows that the  $(200)$  peak of the newly formed fcc-structural phase is located at  $43.6^\circ$  ( $2\theta$ ), while that of the TiN impurity in  $\text{Ti}_4\text{AlN}_3$  is located at  $42.6^\circ$  ( $2\theta$ ), as shown in Fig. 3(g). The coexistence of these two distinguishable  $(200)$  peaks further indicates that the newly formed fcc phase is structural distinct from binary TiN.

Figures 7(a)–7(f) show the proposed structures and atomic arrangements along  $[1\bar{1}0]$  of the three corresponding fcc-structured phases [i.e., fcc-TiC, fcc- $\text{Ti}_3(\text{AlC}_2)$ , and fcc- $(\text{Ti}_3\text{Al})\text{C}_2$ ]. In the XRD patterns simulated using these structures [Fig. 7(g)], the  $(111)$ ,  $(200)$ , and  $(220)$  peaks of each are located at the same  $2\theta$  angles when their unit cell parameters are set to the same value. However, due to the different locations of the Al atoms in the structure, the relative intensities of these peaks differ. In all the experimental XRD patterns shown in Fig. 3 and those found elsewhere in the literature,<sup>98–101,103,132–135</sup> the intensity of the  $(111)$  peak is higher than that of the  $(200)$  peak and the  $(220)$  peak. This is consistent with the simulation results for the fcc- $(\text{Ti}_3\text{Al})\text{C}_2$  phase in Fig. 7(g), indicating that this is the most likely structure of the fcc phase. Additionally, *ab initio* simulation results

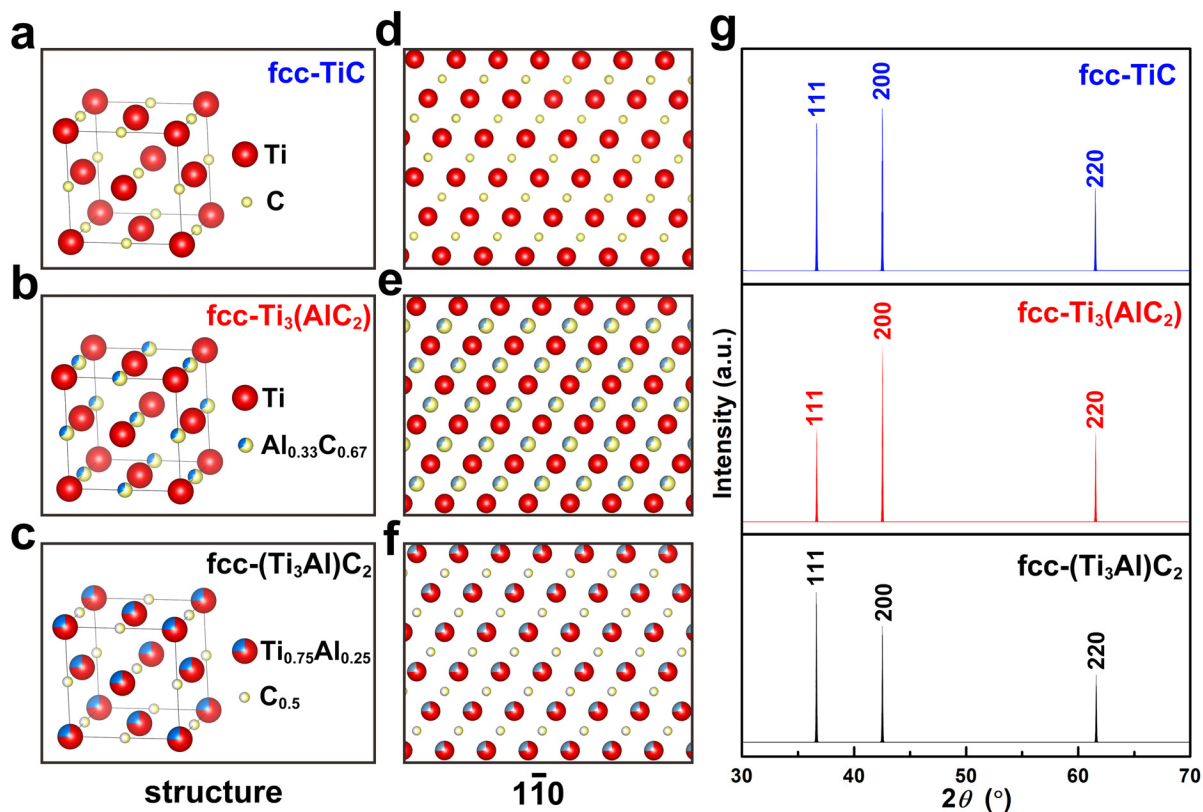


**FIG. 7.** Unit cells of (a) fcc-TiC, (b) fcc-Ti<sub>3</sub>(AlC<sub>2</sub>), and (c) fcc-(Ti<sub>3</sub>Al)C<sub>2</sub>, and [(d)–(f)] the corresponding atomic arrangements along [1-10]. (g) Simulated XRD patterns of these three proposed structures. The relative peak intensity in the simulated pattern obtained based on structure of fcc-(Ti<sub>3</sub>Al)C<sub>2</sub> (c) is consistent with the experimental results.

16 April 2024 01:28:24

show that fcc-M<sub>n+1</sub>(AX<sub>n</sub>) is energetically stable and its equilibrium unit cell parameters are consistent with those obtained from experimental XRD measurements.<sup>47</sup> Thus, the transformation to a new fcc-structured (M<sub>n+1</sub>A)X<sub>n</sub> phase is the most reasonable among these three (a-c) mechanisms.

### C. High-temperature effects on structural evolution

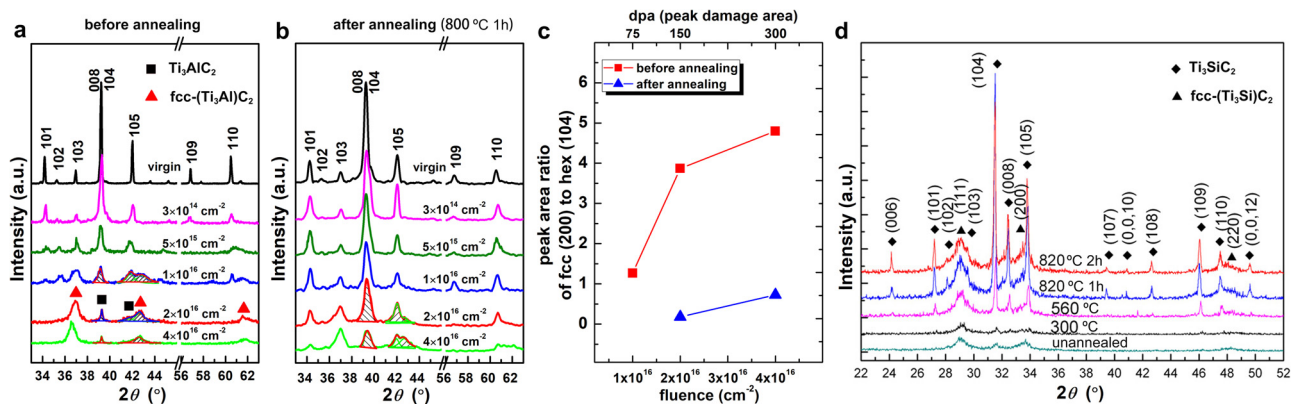
The discussion above focuses on room temperature effects of radiation. As the temperature increases either during irradiation or after (heat treatment), atomic migration barriers decrease relative to those at room temperature, such that atoms and defects move more rapidly. Therefore, the radiation-induced defects become more likely to annihilate one another, and the damage induced by irradiation can be partially recovered.

Figures 8(a) and 8(b) show the XRD patterns of MAX phase samples irradiated with 1 MeV Au<sup>+</sup> ions at room temperature, as well as patterns collected from these samples after post-irradiation annealing at 800 °C for 1 h. As expected for a room temperature irradiation, phase transformation from the initial hexagonal phase to the fcc-(Ti<sub>3</sub>Al)C<sub>2</sub> phase was observed. After annealing, the newly formed fcc phase partially transforms back to the hexagonal phase. By analyzing the area ratio of the (111) peak of the fcc phase to that of the (006) peak of the hexagonal phase, the extent of irradiation-induced

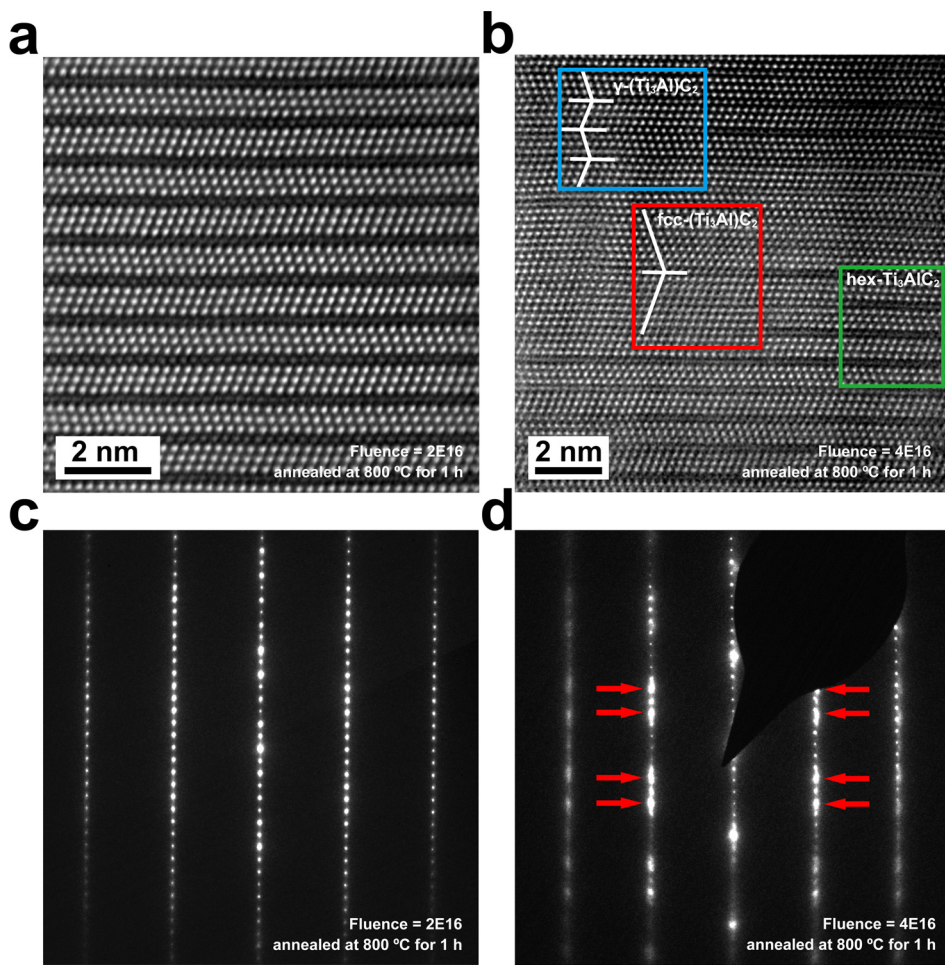
transformation, at various fluences, can be qualitatively assessed, as shown in Fig. 8(c). These results indicate the sluggish growth of the fcc phase under irradiation at room temperature and apparent recovery to the hexagonal structure after annealing, despite the retention of a small amount of residual fcc phase. However, another important question arises: do the Al atoms migrate back to their initial locations during recovery, or do they remain uniformly distributed among the cation sites alongside Ti atoms in the hexagonal structure?

Figure 9 shows STEM HAADF images and the corresponding SAED patterns of MAX phases irradiated with 1 MeV Au<sup>+</sup> ions irradiated to fluences of  $2 \times 10^{16}$  and  $4 \times 10^{16} \text{ cm}^{-2}$  after annealing at 800 °C for 1 h. The fcc-(Ti<sub>3</sub>Al)C<sub>2</sub> solid solution formed at  $2 \times 10^{16} \text{ cm}^{-2}$  almost completely transforms back to the initial hexagonal Ti<sub>3</sub>AlC<sub>2</sub> phase. In the recovered hexagonal phase, Ti and Al atoms occupy their initial locations instead of remaining mixed with one another. Even at a higher ion fluence of  $4 \times 10^{16} \text{ cm}^{-2}$ , partial recovery of the structure was observed after annealing. Following annealing, all three fcc-(Ti<sub>3</sub>Al)C<sub>2</sub>,  $\gamma$ -(Ti<sub>3</sub>Al)C<sub>2</sub>, and Ti<sub>3</sub>AlC<sub>2</sub> phases coexist in this case. Therefore, the phase transformation from hexagonal Ti<sub>3</sub>AlC<sub>2</sub> to  $\beta$  to  $\gamma$  to fcc-(Ti<sub>3</sub>Al)C<sub>2</sub> phase is reversible after annealing.

Similar behavior has been reported in Ti<sub>3</sub>SiC<sub>2</sub> irradiated with 2 MeV I<sup>2+</sup>, 700 keV C<sup>+</sup>, and 110 keV He<sup>+</sup> ions, as shown in Fig. 8(d).<sup>98,101,136</sup> These works demonstrate the temperature dependence



**FIG. 8.** Representative GIXRD patterns from  $\text{Ti}_3\text{AlC}_2$  before and after irradiation with 1 MeV Au ions to fluences ranging from  $3 \times 10^{14} \text{ cm}^{-2}$  to  $4 \times 10^{16} \text{ cm}^{-2}$  (a) at room temperature and (b) after annealing at  $800^\circ\text{C}$  for 1 h. (c) The intensity ratios of fcc (200) and hexagonal (104) peaks as a function of ion fluence. With increasing fluence, the diffraction maxima corresponding to all the initial phases decrease in intensity, as the patterns indicate a transformation from the initial hexagonal structure to the fcc structure. The black squares and the blue triangles represent the peaks corresponding to the initial hexagonal phase and the fcc phases, respectively. After annealing, the structure is substantially recovered. (d) GIXRD pattern from  $\text{Ti}_3\text{SiC}_2$  before and after irradiation with 2 MeV I ions to a fluence of  $3 \times 10^{15} \text{ cm}^{-2}$ , as well as annealing at 300, 560, and  $820^\circ\text{C}$ . Reproduced with permission from Zhang *et al.*, Appl. Surf. Sci. **258**, 6281–6287 (2012). Copyright 2012 Elsevier.



**FIG. 9.** STEM HAADF images and the corresponding SAED patterns of  $\text{Ti}_3\text{AlC}_2$  irradiated with 1 MeV Au ions to fluences of [(a) and (c)]  $2 \times 10^{16} \text{ cm}^{-2}$  and [(b) and (d)]  $4 \times 10^{16} \text{ cm}^{-2}$ , after annealing at  $800^\circ\text{C}$  for 1 h. Following annealing, the structure is completely recovered in the sample irradiated to a fluence of  $2 \times 10^{16} \text{ cm}^{-2}$ , while the structure is partially recovered at the fluence of  $4 \times 10^{16} \text{ cm}^{-2}$ , with hex- $\text{Ti}_3\text{AlC}_2$ ,  $\gamma\text{-}(\text{Ti}_3\text{Al})\text{C}_2$ , and fcc-( $\text{Ti}_3\text{Al})\text{C}_2$  phases coexisting.

of recovery of these materials. For example, in irradiated  $\text{Ti}_3\text{SiC}_2$ , annealing at  $300^\circ\text{C}$  did not alter the fcc-structured phase, an observation attributed to insignificant defect diffusion. When the annealing temperature was increased to greater than  $560^\circ\text{C}$ , the structure partially changed from the fcc phase to the hexagonal phase. This indicates that there exists a critical temperature above which sufficient atomic mobility can lead to recombination of defects and recovery of the structure.

In addition to post-irradiation annealing, many studies have investigated the response of the MAX phases to ion irradiation at elevated temperatures.<sup>24,101,103,110,133,134,136–140</sup> In principle, exposure to high temperatures during irradiation facilitates defect recovery and retards the structural phase evolution, yielding effects similar to post-irradiation annealing.

Representative high-temperature irradiation XRD data are shown in Fig. 10. Despite different radiation conditions (ion type and energy), ion irradiation at room temperature triggers similar phase transformations, from the hexagonal phase to the fcc phase, in  $\text{Ti}_3\text{AlC}_2$ ,  $\text{Ti}_2\text{AlC}$ , and  $\text{Ti}_3\text{SiC}_2$ . As the irradiation temperature increases to around  $300^\circ\text{C}$ , the phase transformation process is slightly hindered due to a limited increase in atomic mobility and defect recombination. For example, in  $\text{Ti}_3\text{AlC}_2$  and  $\text{Ti}_3\text{SiC}_2$ , the phase ratio of the  $\gamma$  phase and fcc phase achieved from irradiation at  $300^\circ\text{C}$  is smaller than that achieved at room temperature. As the irradiation temperature is increased to more than  $500^\circ\text{C}$ , all these compounds exhibit greatly

enhanced phase retention under irradiation, with the initial hexagonal phases remaining dominant. For temperatures in the range  $600\text{--}800^\circ\text{C}$ , phase transformation hardly occurs. Similar effects of temperature on irradiation-induced phase evolution were also found in other MAX phases, such as  $\text{Zr}_2\text{AlC}$ .<sup>140</sup> These results are particularly important with respect to the potential application of MAX phases in nuclear energy systems as temperatures of several hundred  $^\circ\text{C}$  or greater are typical.

Besides the phase transformation process, the defect behaviors under ion or neutron irradiation significantly influence materials' properties and play an important role in designing nuclear materials. Therefore, defect behaviors in the MAX phases at various temperature have also been investigated.<sup>122,133,139,141–143</sup> Although defect evolution in irradiated MAX phases in a complex function of temperature, irradiation conditions, and composition, it can be useful to approximately categorize radiation response, and its temperature dependence, using the homologous irradiation temperature  $T/T_M$ , where  $T_M$  is the melting point.<sup>144–146</sup> From this perspective, there exist three temperature ranges in materials known as stages I, III, and IV, which correspond to the onset temperatures for long-range self-interstitial-atom migration, monovacancy migration, and thermal dissolution of small vacancy clusters, respectively. In these stages, the defect production/recovery mechanisms differ such that different defect behaviors were observed. For example, at temperatures below stage I, ceramics are prone to become amorphous under irradiation due to the immobility of point

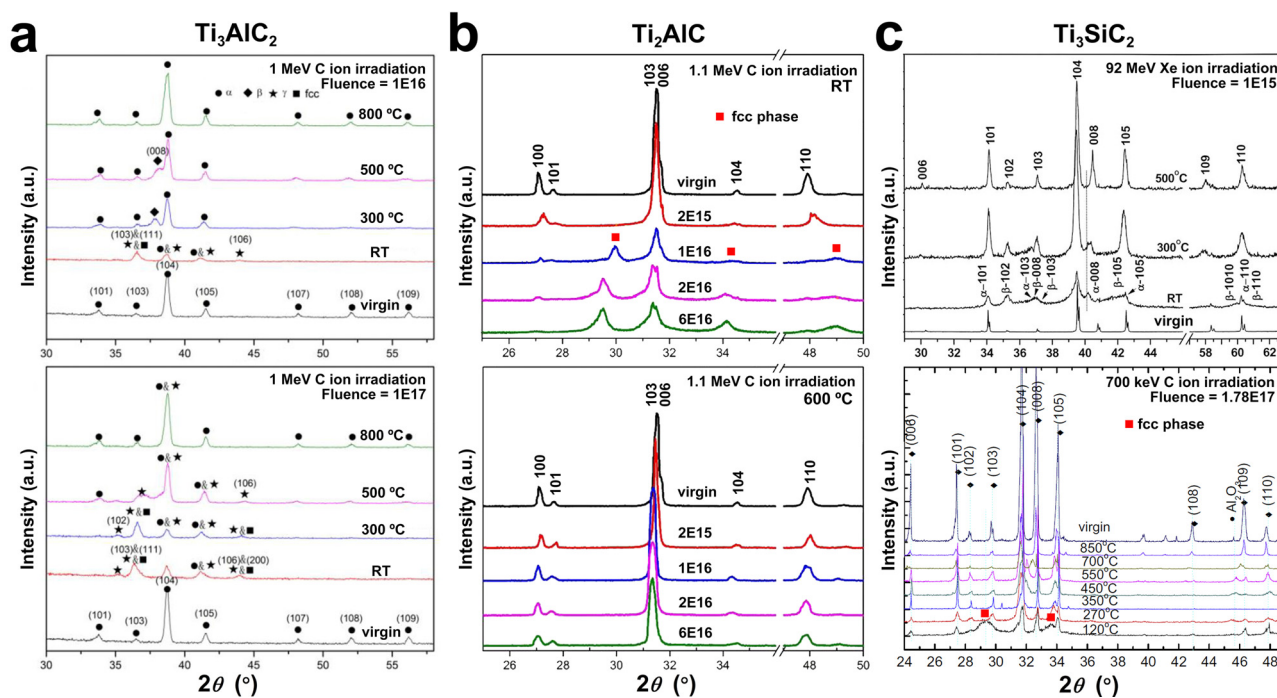


**FIG. 10.** GIXRD patterns of (a)  $\text{Ti}_3\text{AlC}_2$ , (b)  $\text{Ti}_2\text{AlC}$ , and (c)  $\text{Ti}_3\text{SiC}_2$  before and after irradiation with 1 MeV, 1.1 MeV C ions and 92 MeV Xe ions at different temperatures. High-temperature irradiation hinders the phase transformation in all compounds, which is attributed to enhanced atomic migration and annihilation of defects. Reproduced with permission from Deng et al., *Acta Mater.* **189**, 188–203 (2020). Copyright 2020 Acta Materialia, Inc., published by Elsevier Ltd. Reproduced with permission from Liu et al., *Nucl. Instrum. Methods Phys. Res., Sect. B* **406**, 662–669 (2017). Copyright 2017 Elsevier. Reproduced with permission from Liu et al., *Nucl. Instrum. Methods Phys. Res., Sect. B* **268**, 506–512 (2010). Copyright 2009 Elsevier. Reproduced with permission from Qi et al., *Acta Mater.* **66**, 317–325 (2014). Copyright 2013 Acta Materialia, Inc., published by Elsevier Ltd.

defects, whereas at stage III temperatures, void/cavity formation is likely to occur.

Defect behaviors in MAX phases under irradiation at different stages differ. Clark *et al.* employed TEM analysis under two-beam conditions and obtained bright-field and dark-field images of  $\text{Ti}_3\text{AlC}_2$  irradiated to 30 dpa at 400 and 700 °C, using the  $\mathbf{g} \sim \langle 0001 \rangle$  (basal) and  $\mathbf{g} \sim \langle 1\bar{1}00 \rangle$  (prism) diffraction vectors,<sup>133</sup> as shown in Fig. 11. Compared with the pristine structure, there appears a large density of “black spots” or small defect clusters in the area irradiated to 30 dpa at 400 °C, indicating the formation of defect similar to those formed at room temperature, as shown in Fig. 2(a). At 700 °C, the defects in  $\text{Ti}_3\text{AlC}_2$  appear to be comprised of smaller basal defects that coalesce in a stacking sequence at  $\pm 35^\circ$  from the basal direction, as shown in Fig. 11(c). However, in  $\text{Ti}_3\text{SiC}_2$  at the same irradiation condition (30 dpa, 700 °C), the grouped defects exist as large stacking faults along the basal plane and dislocation loops along the prism axis.<sup>133</sup> Additionally, no voids were formed in either material. Similar defect formation behavior is observed in most MAX phases studied under irradiation.<sup>112,140,141</sup> These results suggest that the irradiation temperatures used were between defect recovery stages I and III, characterized by high interstitial mobility and limited vacancy mobility. As the irradiation temperature increases, voids or cavities appeared within the grains or along grain boundaries as small, mobilized vacancies aggregate.<sup>122,142</sup>

#### IV. COMPOSITIONAL TRENDS IN THE SUSCEPTIBILITY OF MAX PHASES TO RADIATION-INDUCED PHASE EVOLUTION

As shown by their chemical formulas, there are four compositional variables that describe the  $M_{n+1}AX_n$  phases: M, A, X, and  $n$ . These parameters determine their physical and mechanical properties,<sup>57,81,147,148</sup> as well as their responses to irradiation and other extreme environments.<sup>47,90,91,93,103,105,108,109,128,133,141,142,149–151</sup> Therefore, investigation of the role of M, A, X, and  $n$  in the MAX phase radiation response, including susceptibility to phase transformation, is critical to understanding the performance of these materials in nuclear applications. However, the systematic study of compositional trends is difficult because much of the experimental work has been done

under different irradiation conditions. Ideally, radiation responses of various MAX phases should be studied under the same irradiation conditions (i.e., ion type, energy, and temperature). This is necessary due to, for example, the different damage production efficiencies achieved by different irradiation conditions (even at the same dpa level), as discussed above. Here, we attempt to clarify systematic compositional trends by reviewing data from the literature on different MAX phases irradiated under identical or analogous conditions.

The most studied MAX phases in terms of radiation effects are  $\text{Ti}_3\text{SiC}_2$  and  $\text{Ti}_3\text{AlC}_2$ , two representative MAX phases in which only the A elements differ. These compounds have been investigated using a variety of irradiation conditions. Comparatively few studies have focused on comparing susceptibility to radiation-induced phase evolution in other MAX phases. Still, seven different MAX phases ( $\text{Ti}_3\text{AlC}_2$ ,  $\text{Ti}_2\text{AlC}$ ,  $\text{Ti}_3\text{SiC}_2$ ,  $\text{V}_2\text{AlC}$ ,  $\text{Cr}_2\text{AlC}$ ,  $\text{Ti}_4\text{AlN}_3$ , and  $\text{Ti}_2\text{AlN}$ ) have been irradiated with 1 MeV  $\text{Au}^+$  ions and characterized, allowing a systematic comparison of compositional trends corresponding to this irradiation condition.<sup>47,104–106,108</sup> Below, we systematically discuss the available data on the role of each compositional parameter—M, A, X and  $n$ —on the response of these materials to irradiation. We conclude that there are two primary factors: bond strength (differing among compositions) and  $n$  (representing differences in atomic structures).

#### A. M atoms

Figures 12(a)–12(l) show SAED patterns and high-resolution TEM images of  $M_2\text{AlC}$  ( $M = \text{Cr}, \text{V}, \text{Ti}$ ) along [1120] following irradiation with 1 MeV  $\text{Au}^+$  ions to fluences of  $1 \times 10^{14}$  and  $1 \times 10^{16} \text{ cm}^{-2}$ . At the lower fluence, phase transformations from the initial hexagonal phases to the  $\gamma$ -( $M_2\text{Al}$ )C phases occur in all three compounds. It should be noted that the atomic configurations along the  $c$  axis in  $\gamma$ -( $\text{Ti}_2\text{Al}$ )C are different from those of  $\gamma$ -( $\text{V}_2\text{Al}$ )C and  $\gamma$ -( $\text{Cr}_2\text{Al}$ )C, as shown in Figs. 12(b), 12(f), and 12(j), such that the diffraction spots in the initial patterns are, for each composition, attenuated in different ways, as shown in Figs. 12(a), 12(e), and 12(i).<sup>104,105</sup> In parallel with this phase transformation,  $\text{Cr}_2\text{AlC}$  becomes partially amorphous under irradiation, as indicated by the white arrow in Fig. 12(a). As the fluence increases to  $1 \times 10^{16} \text{ cm}^{-2}$ , the SAED pattern and HRTEM

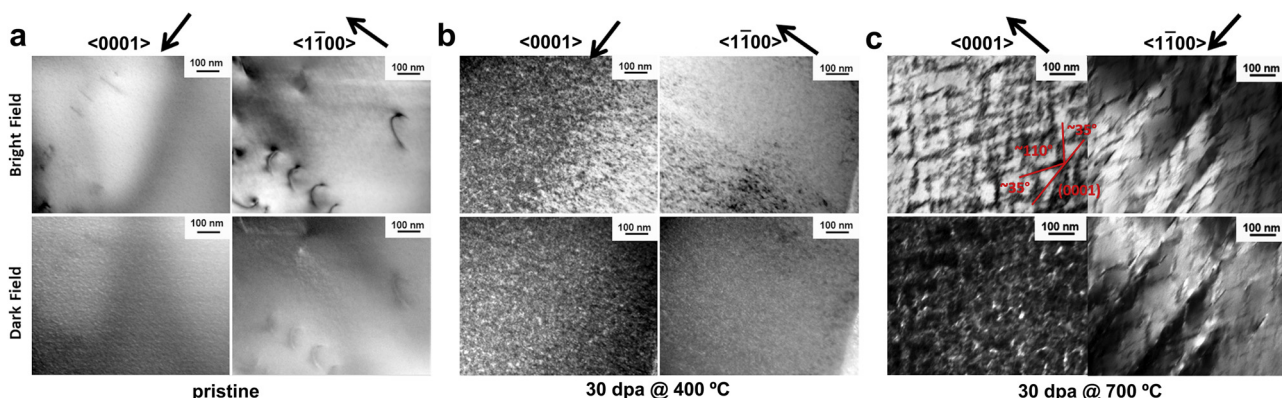


**FIG. 11.** Bright-field (BF) and dark-field (DF) cross-sectional TEM images of  $\text{Ti}_3\text{AlC}_2$  (a) before irradiation and (b) irradiated to 30 dpa at a temperature of 400 °C (c) and irradiated to 30 dpa at a temperature of 700 °C. The basal and prism diffraction vector directions are indicated by  $\langle 0001 \rangle$  and  $\langle 1\bar{1}00 \rangle$ , respectively. Reproduced with permission from Clark *et al.*, *Acta Mater.* **105**, 130–146 (2016). Copyright 2015 Acta Materialia, Inc., published by Elsevier Ltd.

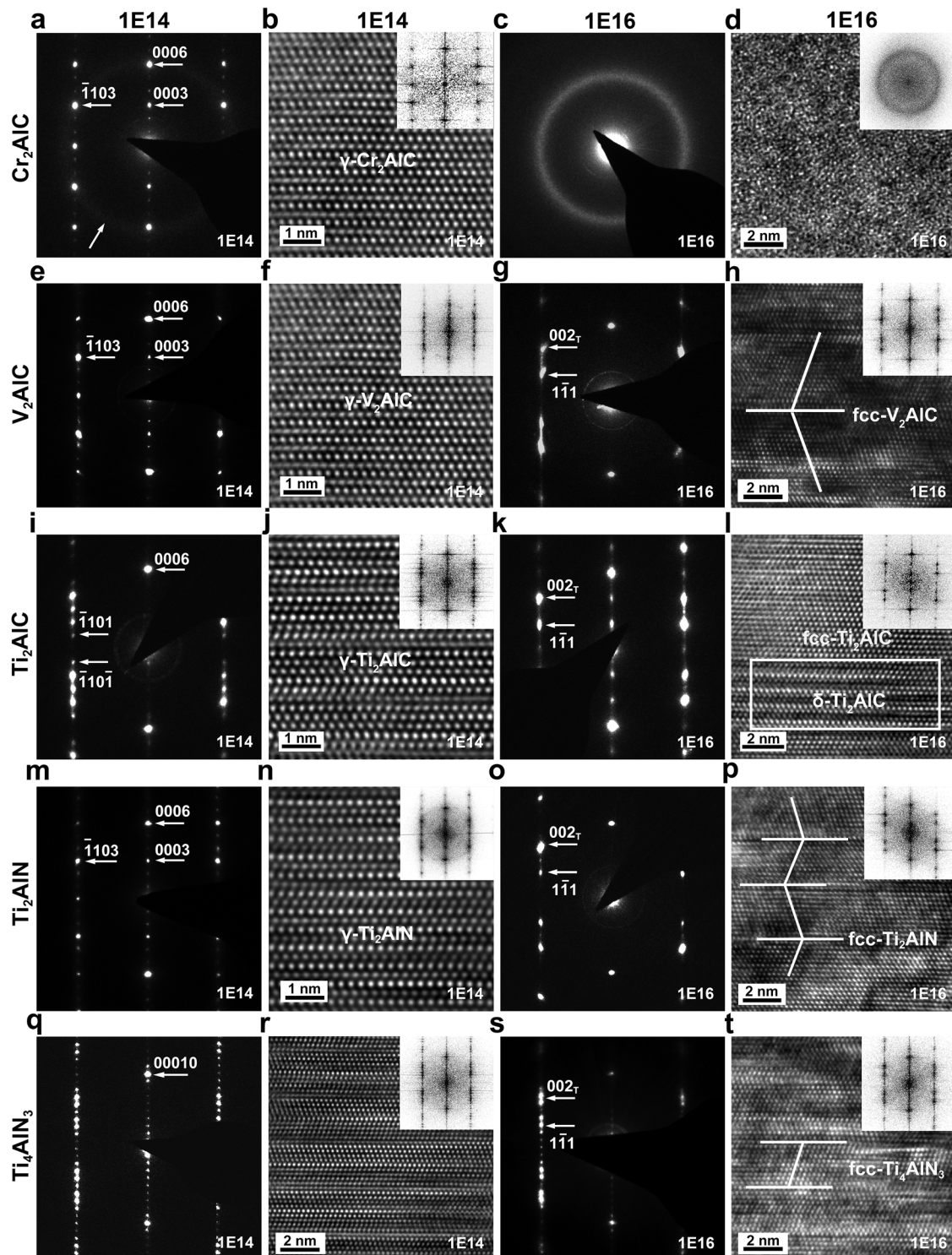


**FIG. 12.** SAED patterns and the corresponding high-resolution TEM images of [(a)–(d)] Cr<sub>2</sub>AlC, [(e)–(h)] V<sub>2</sub>AlC, [(i)–(l)] Ti<sub>2</sub>AlC, [(m)–(p)] Ti<sub>2</sub>AlN, and [(q)–(t)] Ti<sub>4</sub>AlN<sub>3</sub> after 1 MeV Au ion irradiation to fluences of  $1 \times 10^{14}$  and  $1 \times 10^{16} \text{ cm}^{-2}$ . Reproduced with permission from Wang *et al.*, *Acta Mater.* **98**, 197–205 (2015). Copyright 2015 Acta Materialia, Inc., published by Elsevier Ltd. Reproduced with permission from Wang *et al.*, *Acta Mater.* **144**, 432–446 (2018). Copyright 2017 Acta Materialia, Inc., published by Elsevier Ltd. Reproduced with permission from Wang *et al.*, *J. Am. Ceram. Soc.* **99**(5), 1769–1777 (2016). Copyright 2016 The American Ceramic Society.

image of Cr<sub>2</sub>AlC [Figs. 12(c) and 12(d)] both show that this material is completely amorphized by irradiation. In contrast, V<sub>2</sub>AlC transforms from the  $\gamma$  phase to the nano-twinned fcc-(V<sub>2</sub>Al)C solid solution, as shown in Figs. 12(g) and 12(h). Ti<sub>2</sub>AlC exhibits formation of both the fcc phase and a metastable phase that is transformed from the  $\gamma$  phase, denoted as the  $\delta$  phase.<sup>104</sup> This material completely transforms to the fcc phase as the fluence further increases to  $2 \times 10^{16} \text{ cm}^{-2}$ . These microscopy results are consistent with those of GIXRD measurements, as shown in Fig. 3. They indicate that the M factor plays a critical role in the susceptibility of MAX phases to irradiation-induced phase transformation or amorphization. Ti<sub>2</sub>AlC exhibits the highest resistance to irradiation-induced structural alteration, while Cr<sub>2</sub>AlC is the most sensitive. V<sub>2</sub>AlC exhibits intermediate radiation tolerance.

In previous first-principles simulations,<sup>90,91</sup> it has been argued that the formation energy of cationic antisite defects is an important criterion for the radiation tolerance of the MAX phases. MAX phases with lower antisite formation energies typically exhibit higher resistance to irradiation-induced structural evolution. This is due to the easy exchange of M and A atoms, which provides an efficient means for the accommodation of radiation-induced point defects produced during irradiation. However, Xiao *et al.*<sup>93</sup> calculated the formation energies of various kinds of Frenkel pairs and antisite defects in Ti<sub>2</sub>AlC and Cr<sub>2</sub>AlC. The formation energy of the Ti/Al antisite defect in Ti<sub>2</sub>AlC is 2.52 eV, greater than that of the Cr/Al antisite defect (2.40 eV) in Cr<sub>2</sub>AlC. This suggests that Cr<sub>2</sub>AlC should be less susceptible to irradiation-induced structural evolution, when in fact the

experimental work discussed above showed Cr<sub>2</sub>AlC to be more susceptible to these processes than Ti<sub>2</sub>AlC. The failure of this antisite defect formation energy criterion to accurately predict the radiation responses of the MAX phases might be attributed to the roles of other defects in the corresponding phase transformations. In other words, although antisite defects are the lowest energy defects in MAX phases, they alone are insufficient for explaining compositional trends in MAX phase radiation response. Therefore, comparison of the formation energies of other defects is needed. For example, Christopoulos *et al.* investigated the defect processes of M<sub>3</sub>AlC<sub>2</sub> (M = V, Zr, Ta, Ti) and found that carbon Frenkel pair formation also impacts structural stability under irradiation.<sup>152</sup>

In addition to defect formation energies, resistance to structural disorder or amorphization under irradiation may also be explained by bond character.<sup>153</sup> Xiao *et al.* have assessed the role of bond type on the radiation response of M<sub>2</sub>AlC (M = Ti, V, Cr) compounds.<sup>93</sup> For all three compounds, calculated density of states (DOS) results show that there is a high degree of hybridization of M(3d) orbitals and C(2p) orbitals, indicating a strong covalent interaction in M-C bonds, as shown in Figs. 13(a)–13(c). The hybridization of M-Al and M-C bonds in Ti<sub>2</sub>AlC is closer to the Fermi level ( $E_F$ ) than those of V<sub>2</sub>AlC and Cr<sub>2</sub>AlC, indicating less covalent bonding characters between these bonds in Ti<sub>2</sub>AlC than those in V<sub>2</sub>AlC and Cr<sub>2</sub>AlC. This is further confirmed by the calculated electron density distribution, shown in Fig. 14. The densities located in the Ti-Al and the Ti-C regions are smaller than those of the M-Al and M-C regions, respectively,

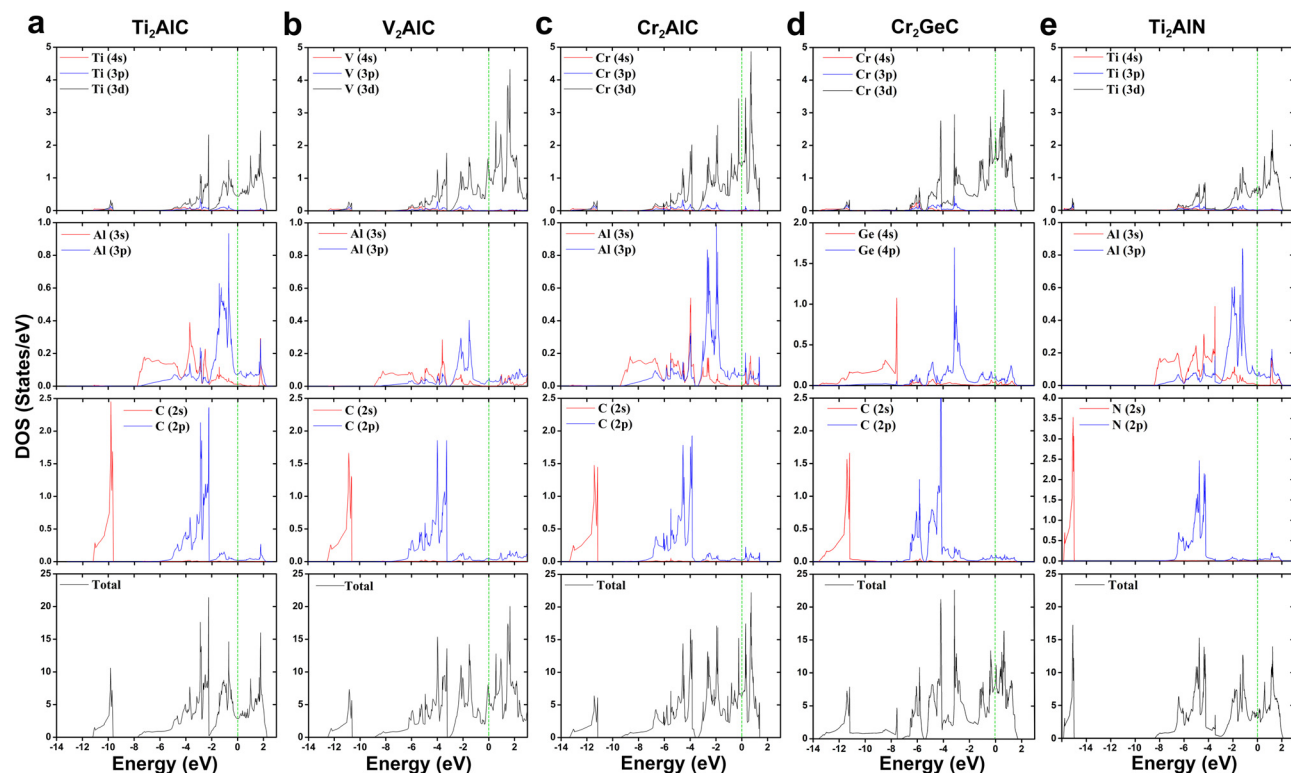
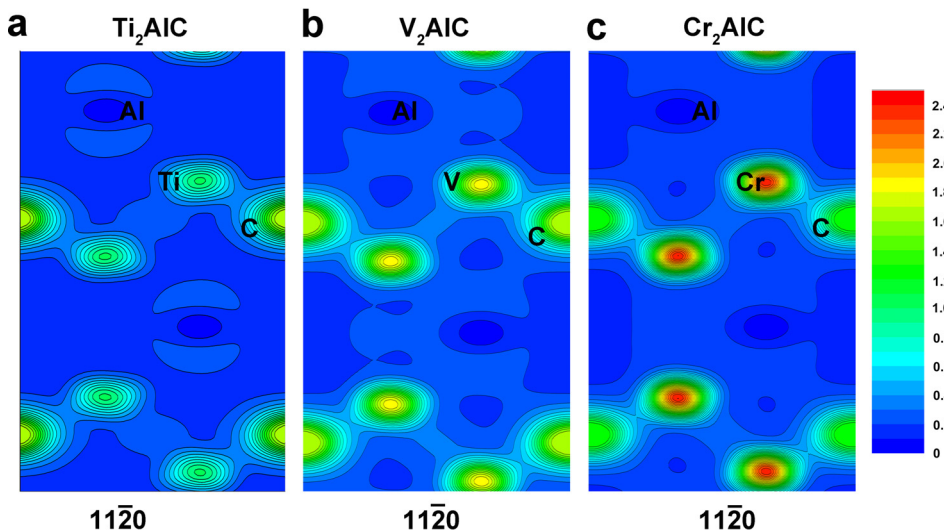


FIG. 13. Calculated density of states and partial density of states for (a) Ti<sub>2</sub>AlC, (b) V<sub>2</sub>AlC, (c) Cr<sub>2</sub>AlC, (d) Cr<sub>2</sub>GeC, and (e) Ti<sub>2</sub>AlN. The green line is plotted to indicate DOS at the Fermi level. Reproduced with permission from Xiao *et al.*, J. Am. Ceram. Soc. **98**(4), 1323–1331 (2014). Copyright 2015 The American Ceramic Society.



**FIG. 14.** Distribution of electron charge density on the  $(11\bar{2}0)$  plane for (a)  $Ti_2AlC$ , (b)  $V_2AlC$ , and (c)  $Cr_2AlC$ . The unit of the given charge density is  $e/\text{\AA}^3$ . Reproduced with permission from Xiao *et al.*, J. Am. Ceram. Soc. 98(4), 1323–1331 (2014). Copyright 2015 The American Ceramic Society.

indicating that Ti-Al and Ti-C bonds are less covalent than M-Al and M-C bonds in  $V_2AlC$  and  $Cr_2AlC$ . Bond covalency can serve as a useful proxy for bond strength, since covalent bonds are relatively strong, suggesting that lattice distortion in compounds with stronger covalent bonds (i.e.,  $Cr_2AlC$ ) is less likely to occur. In contrast, the weaker, more ionic bonding of Ti-Al in  $Ti_2AlC$  allows for easier lattice distortion, and therefore the incorporation of defects into the crystalline lattice. These results indicate that  $Ti_2AlC$  should be the least susceptible to irradiation-induced structural disordering among these three compounds, assuming that bonding character is the primary factor determining structural stability under irradiation. This compositional trend is consistent with the experimental results  $M_2AlC$  ( $M = Ti, V, Cr$ ).<sup>104,105</sup>

This bonding character criterion serves as an effective predictor of the susceptibility of MAX phases to radiation-induced structural evolution. To validate its predictive power and its utility for the design of MAX phase materials for use in nuclear applications, research on additional MAX phases should be completed. For example, interatomic bonding is weaker in  $Zr_2AlC$  than in  $Cr_2AlC$ , suggesting that the former should be less susceptible to irradiation-induced phase transformation or amorphization.<sup>154</sup>

### B. A atoms

MAX phases with different A compositions exhibit different radiation effects. For example, Whittle *et al.* first employed *in situ* TEM irradiation to study  $Ti_3SiC_2$  and  $Ti_3AlC_2$ .<sup>149</sup> Their results show that  $Ti_3SiC_2$  becomes partially amorphous under 1 MeV  $Xe^{2+}$  ion irradiation, while  $Ti_3AlC_2$  remains crystalline, as shown in Figs. 15(a) and 15(b). This indicates that  $Ti_3SiC_2$  is more susceptible to irradiation-induced amorphization.

Using the same method, Bugnet *et al.* studied the amorphization process in  $Cr_2AC$  ( $A = Al$  or  $Ge$ ) under irradiation, as shown in Figs. 15(c)–15(f).<sup>128</sup> Both compounds become amorphous after irradiation to relatively low fluence, yet the threshold fluence at which amorphization occurred in  $Cr_2AlC$  was higher than that of  $Cr_2GeC$ . Specifically,

at a fluence of  $1 \times 10^{14} \text{ cm}^{-2}$ ,  $Cr_2GeC$  became partially amorphous, while  $Cr_2AlC$  remained crystalline.

More recently, Zhao and Xiao *et al.* analyzed the interatomic bonding characters of  $Ti_3SiC_2$  and  $Ti_3AlC_2$ .<sup>91,93</sup> The DOS plot (Fig. 16) reveals weaker bonding between Ti-Al than between Ti-Si as hybridization of the former is much closer to  $E_f$  than that of the latter. This difference might be attributed to the fact the Al atom has one less valence electron and larger metallicity than the Si atom. The different bonding character between Ti-Al and Ti-Si is further verified by the electron density distribution (Fig. 17), which shows that the density located in the Ti-Al region is much smaller than that of the Ti-Si region. All these calculation results indicate that  $Ti_3AlC_2$  is more resistant to irradiation-induced amorphization than is  $Ti_3SiC_2$ , which is consistent with experimental results (Figs. 3 and 15). Likewise, the Cr-Ge in  $Cr_2GeC$  is more covalent than Cr-Al in  $Cr_2AlC$ , suggesting that  $Cr_2GeC$  will be more susceptible to the irradiation-induced amorphization than  $Cr_2AlC$ , as shown in Figs. 13(c) and 13(d). This is consistent with the experimental results, shown in Figs. 15(c)–15(f).

### C. X atoms

Only limited research has directly compared the radiation responses of MAX phases with different X elements. Recently, the responses of  $Ti_2AlC$  and  $Ti_2AlN$  to 1 MeV  $Au^+$  ions were investigated.<sup>108</sup> XRD and TEM results showed that the susceptibilities of  $Ti_2AlN$  and  $Ti_2AlC$  to radiation-induced phase transitions from hcp to fcc structures are comparable. However,  $Ti_2AlC$  was slightly more resistant to the radiation-induced phase transition, exhibiting a slightly lower transformation rate as a function of ion fluence, as shown in Figs. 3 and 12. The calculated DOS plots [Figs. 13(a) and 13(e)] of these materials demonstrate that the Ti-Al bond is slightly more ionic in  $Ti_2AlC$  compared with that of  $Ti_2AlN$ . Accordingly, both experimental and computational results show that  $Ti_2AlC$  exhibits a slightly superior radiation tolerance than  $Ti_2AlN$ . The radiation tolerance of other similar compounds could be also estimated by comparing their bond strength, as with in  $Ti_2CdC$  and  $Ti_2CdN$ .<sup>155</sup>

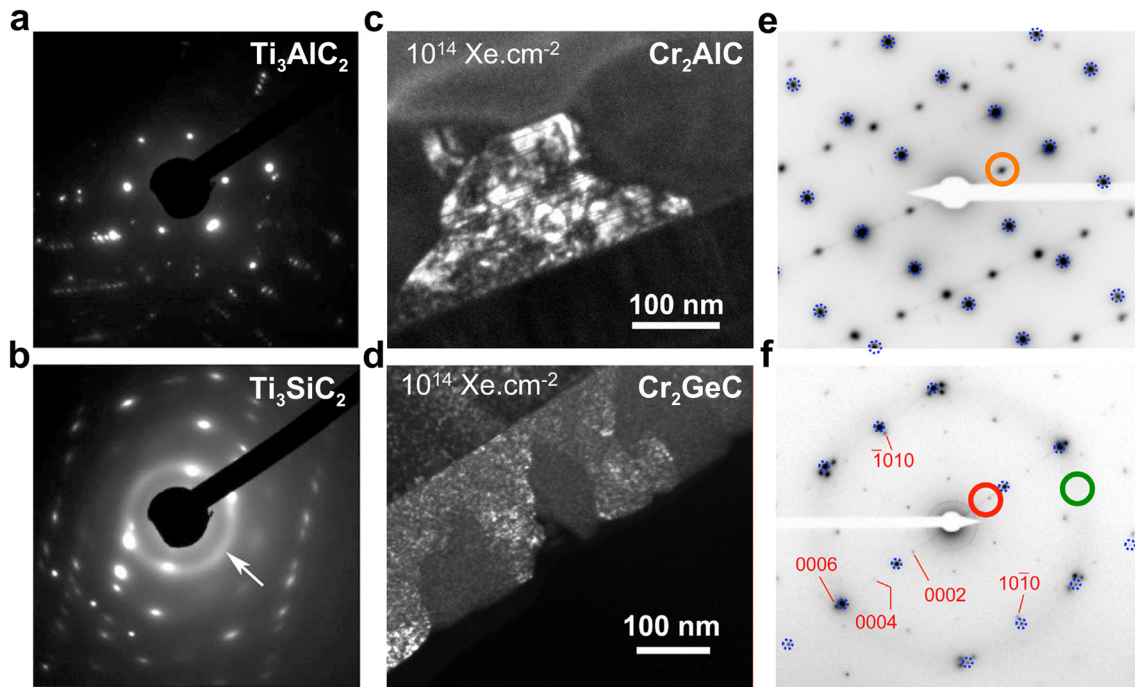


**FIG. 15.** SAED patterns of (a)  $\text{Ti}_3\text{AlC}_2$  and (b)  $\text{Ti}_3\text{SiC}_2$  after 1 MeV Xe ion irradiation to a fluence of  $6.25 \times 10^{15} \text{ cm}^{-2}$ . The white arrow in (b) shows evidence of amorphization. Reproduced with permission from Whittle *et al.*, *Acta Mater.* **58**, 4362–4368 (2010). Copyright 2010 Acta Materialia, Inc., published by Elsevier Ltd. [(c) and (d)] DF TEM images of  $\text{Cr}_2\text{AlC}$  and  $\text{Cr}_2\text{GeC}$  after Xe ion irradiation to a fluence of  $1 \times 10^{14} \text{ cm}^{-2}$ , and [(e) and (f)] the corresponding SAED patterns, indicating differences in their resistance to amorphization induced by ion irradiation. Reproduced with permission from Bugnet *et al.*, *J. Nucl. Mater.* **441**, 133–137 (2013). Copyright 2013 Elsevier.

#### D. $n$

Based on the bond character criterion for radiation tolerance, we expect MAX phases with weaker bond covalence is less susceptible to the irradiation-induced structural evolution. However, variation in the  $n$  value has minimal effect on bond strength, so this criterion alone tells us little about the relative radiation tolerance of materials like  $\text{Ti}_2\text{AlC}$  and  $\text{Ti}_3\text{AlC}_2$ , or  $\text{Ti}_2\text{AlN}$  and  $\text{Ti}_4\text{AlN}_3$ . Therefore, additional factors are necessary to explain composition trends in the radiation tolerance of MAX phases.

As shown in Figs. 3(a), 3(b), 3(g), and 3(h), phase transformations from initial hexagonal structures to fcc solid solution structures were observed in  $\text{Ti}_2\text{AlC}$ ,  $\text{Ti}_3\text{AlC}_2$ ,  $\text{Ti}_2\text{AlN}$ , and  $\text{Ti}_4\text{AlN}_3$ . However, the threshold fluence at which this phase transformation occurs differs as a function of  $n$ . For example, after irradiation to a fluence of  $1 \times 10^{16} \text{ cm}^{-2}$ ,  $\text{Ti}_2\text{AlN}$  almost completely transforms to the fcc phase, while the hexagonal phase remains dominant in  $\text{Ti}_4\text{AlN}_3$ , as has been further confirmed by TEM imaging [Figs. 12(m)–12(t)]. Likewise, the results also show that this phase transformation occurs in  $\text{Ti}_2\text{AlC}$  at a lower fluence than in  $\text{Ti}_3\text{AlC}_2$ . This suggests that for both C-based and N-based MAX phases, compounds with larger  $n$  value are more resistant to the irradiation-induced structural evolution.

Structurally, MAX phases like  $\text{Ti}_2\text{AlC}$  and  $\text{Ti}_3\text{AlC}_2$ , or  $\text{Ti}_2\text{AlN}$  and  $\text{Ti}_4\text{AlN}_3$ , differ in the number of Ti layers interleaved between the close-packed Al layers (i.e., two layers in  $\text{Ti}_2\text{AlC}$  and three layers in  $\text{Ti}_3\text{AlC}_2$ , or 2 layers in  $\text{Ti}_2\text{AlN}$  and four layers in  $\text{Ti}_4\text{AlN}_3$ ). Al atoms most readily migrated along Al layers under irradiation.<sup>156</sup> Therefore, because MAX phases with higher  $n$  value have a lower ratio of Al

layers to Ti layers, they are less susceptible to irradiation-induced phase transformations.

Given that ion irradiation triggers phase transformation to fcc-structured solid solutions for both the 211 and 312 materials, the fcc phases of these compounds must exhibit different cation and anion site occupancies. For example, in 211 MAX phases, fcc solid solutions are considered as fcc-( $\text{Ti}_2\text{Al}$ )X, or fcc-( $\text{Ti}_{0.67}\text{Al}_{0.33}$ )X<sub>0.33</sub>, in which Ti and Al atoms uniformly occupy the cation sites with an occupancy ratio of 2:1 and X atoms occupy the anion sites with the vacancy ratio of 0.67. Likewise, the fcc- $\text{Ti}_3\text{AlC}_2$  and the fcc- $\text{Ti}_4\text{AlN}_3$  phases are also regarded as solid solutions [i.e., fcc-( $\text{Ti}_{0.75}\text{Al}_{0.25}$ )C<sub>0.5</sub> and fcc-( $\text{Ti}_{0.8}\text{Al}_{0.2}$ )N<sub>0.6</sub>]. Therefore, the main structural differences between fcc-( $\text{Ti}_{0.67}\text{Al}_{0.33}$ )N<sub>0.33</sub> and fcc-( $\text{Ti}_{0.8}\text{Al}_{0.2}$ )N<sub>0.6</sub> solid solutions are the Al occupancy (0.33 vs 0.2) and the N vacancy ratio (0.67 vs 0.4). The higher Al occupancy in fcc-( $\text{Ti}_{0.67}\text{Al}_{0.33}$ )N<sub>0.33</sub> leads to more severe structural distortion due to the size difference between Ti and Al cations.<sup>157</sup> Furthermore, the higher X anion vacancy ratio in fcc-( $\text{Ti}_{0.67}\text{Al}_{0.33}$ )N<sub>0.33</sub> decreases the stability of the material, driving irradiation-induced structural evolution.<sup>158</sup> In addition, the occupancy at the cation and anion sites significantly affects the unit cell parameters of the fcc solid solutions, which serves as further evidence of irradiation-induced order-disorder transformations, as opposed to decomposition.<sup>47</sup> Ultimately, the available data show that MAX phases with larger  $n$  values exhibit better structural stability and are less susceptible to irradiation-induced phase transformation due to their lower content and lower anion vacancy ratio in the fcc-structured solid solutions.

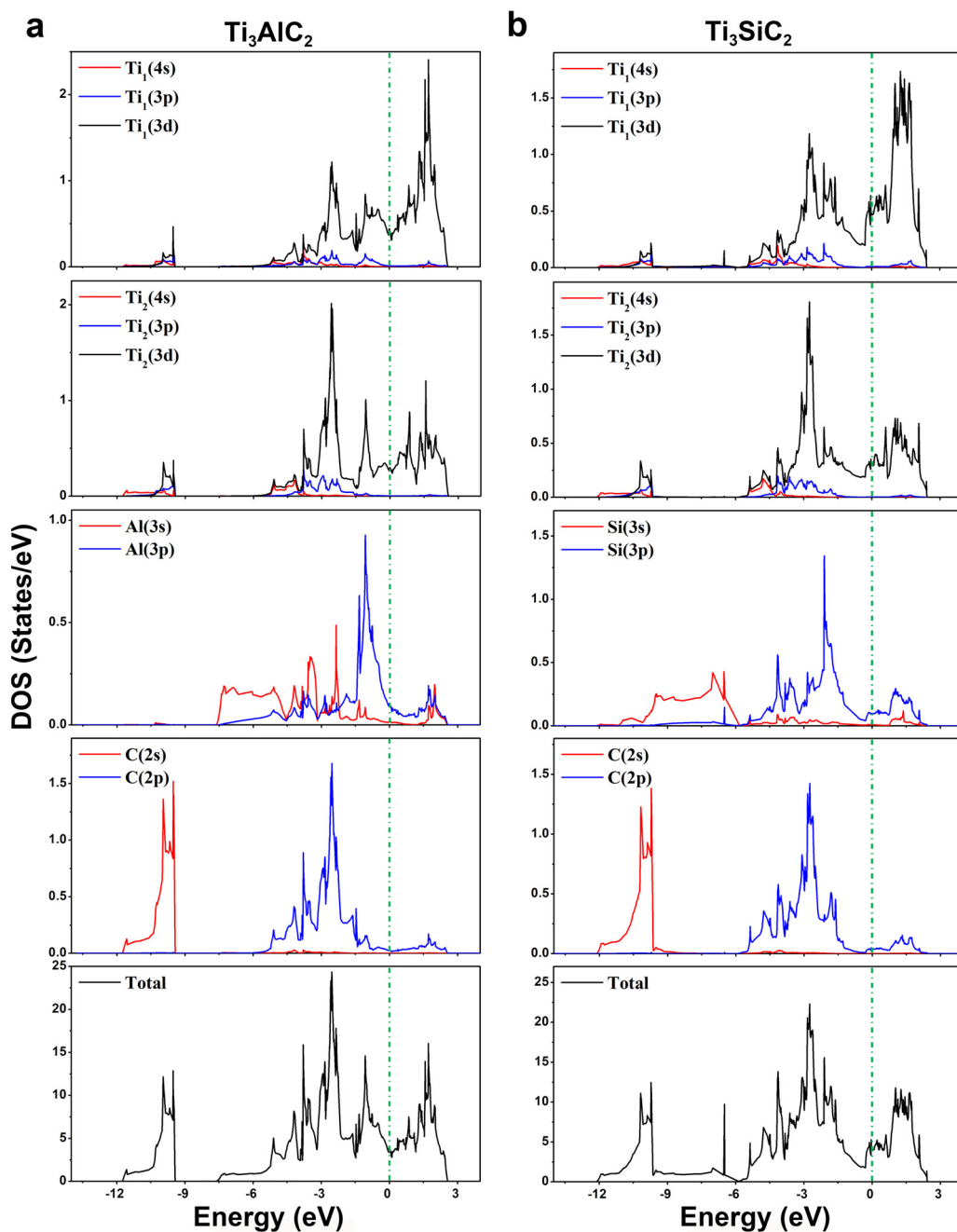


**FIG. 16.** Calculated density of states and partial density of states for (a)  $\text{Ti}_3\text{AlC}_2$  and (b)  $\text{Ti}_3\text{SiC}_2$ . The green line is plotted to indicate DOS at the Fermi level. Reproduced with permission from Zhao *et al.*, J. Appl. Phys. **115**, 023503 (2014). Copyright 2014 AIP Publishing LLC.

However, the energy range of hybridization states may not be accurate for comparison of bond strengths in different compounds. Therefore, alternative measures of bond strength may prove useful. Recently, the bond stiffness of MAX phases has been studied to obtain more accurate and quantitative comparisons among different

compounds. For example, Bai *et al.*<sup>159</sup> investigated the bond stiffness in  $\text{Cr}_2\text{AlB}_2$ ,  $\text{Cr}_3\text{AlB}_4$ ,  $\text{Cr}_4\text{AlB}_6$ , and  $\text{CrAlB}$ , accurately predicting the phase stability and anisotropic behavior based on the estimated bond stiffness. This theoretical model of bond stiffness provides another measure of bond strength, and therefore of the damage tolerance of

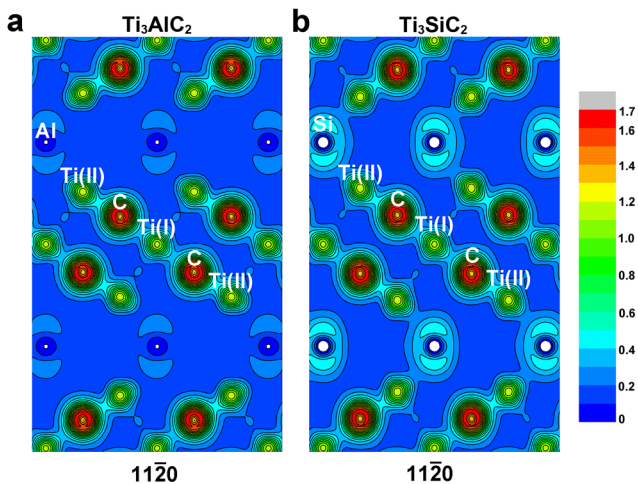


**FIG. 17.** Distribution of electron charge density on the  $(11\bar{2}0)$  plane for (a)  $\text{Ti}_3\text{AlC}_2$  and (b)  $\text{Ti}_3\text{SiC}_2$ . The unit of the given charge density is  $\text{e}/\text{\AA}^3$ . Reproduced with permission from Zhao *et al.*, J. Appl. Phys. 115, 023503 (2014). Copyright 2014 AIP Publishing LLC.

different MAX and related phases. In future work, bond stiffness should be considered alongside other measures of bond strength to evaluate the radiation tolerance of these materials.

## V. PROPERTIES OF THE MAX PHASES AFTER IRRADIATION

The formation of defects induced by irradiation not only triggers phase transformations in the MAX phases, but also induces alteration of their properties: mechanical, electric, and thermal.

### A. Mechanical properties

The MAX phases experience structural expansion during irradiation,<sup>24,113,124,133,142,150,151,160–162</sup> an effect common to almost all other ceramic materials used in nuclear applications, such as simple binary oxides,<sup>163,164</sup> complex oxides,<sup>95,164</sup> and silicon carbides.<sup>165</sup> Due to their unique structures, the MAX phases exhibit anisotropic lattice expansion and swelling. Liu *et al.*<sup>24</sup> first measured the *c* unit cell parameters of  $\alpha\text{-Ti}_3\text{Si}_{0.9}\text{Al}_{0.1}\text{C}_2$  after 92 MeV Xe and 74 MeV Kr ion irradiation at various temperatures using Rietveld refinement. Nappé *et al.*<sup>124</sup> investigated variation of the *a* and *c* unit cell parameters and the unit cell volumes of Ti<sub>3</sub>SiC<sub>2</sub> after irradiation, with their selected results shown in Fig. 18.

More recently, the unit cell expansion behavior of other MAX phases was studied, including Ti<sub>2</sub>AlC,<sup>133</sup> Cr<sub>2</sub>AlC,<sup>129</sup> Zr<sub>3</sub>AlC<sub>2</sub>, Nb<sub>4</sub>AlC<sub>3</sub>, and (Zr<sub>0.5</sub>Ti<sub>0.5</sub>)<sub>3</sub>AlC<sub>2</sub>.<sup>151</sup> Ang *et al.* compiled most of the lattice parameter data as a function of damage level under ion and neutron irradiation for Ti<sub>3</sub>SiC<sub>2</sub><sup>166</sup> and Ti<sub>3</sub>AlC<sub>2</sub>.<sup>161</sup> Nearly all of these reports demonstrate a decrease in the *a* unit cell parameters and an increase in the *c* unit cell parameters with increasing irradiation fluence/dose. As a result of the variation of both the *a* and *c* unit cell parameters, the unit cell volume increases with fluence/dose. The anisotropy of unit cell expansion can be attributed to the formation of specific defects. Ward *et al.*<sup>113</sup> calculated changes in *a* and *c* unit cell parameters induced by formation of the carbon-Frenkel defects and

antisite defects, showing that carbon-Frenkel defects in Ti<sub>3</sub>SiC<sub>2</sub> cause an increase in both *a* and *c* unit cell parameters, while antisite defects cause a decrease in the *a* unit cell parameter and increase in the *c* unit cell parameter. This suggests that antisite defects play a dominant role in defect formation in these materials in accordance with the TEM results discussed previously. In Ti<sub>3</sub>AlC<sub>2</sub>, both defects cause a decrease in the *a* unit cell parameter and an increase in the *c* unit cell parameter.<sup>113</sup>

The expansion of the unit cells leads to microstrain [Fig. 18(d)] and volumetric swelling,<sup>160</sup> with the extent of each depending on irradiation temperature. As the irradiation temperature increases, defect production is suppressed, leading to less variation of the unit cell parameters and volume.

Volumetric swelling through amorphization, point defect production, void swelling, and bubble formation is a critical factor in nuclear materials design. Usually, dimensional changes should be kept below 5 vol. %.<sup>133</sup> The total volumetric swelling in Ti<sub>3</sub>SiC<sub>2</sub>, Ti<sub>3</sub>AlC<sub>2</sub>, and Ti<sub>2</sub>AlC (<2 vol. %) is slightly smaller than that in other traditional structural ceramics, including SiC and Al<sub>2</sub>O<sub>3</sub>.<sup>133</sup>

However, the anisotropic unit cell expansion in the MAX phase leads to cracking (especially intergranular cracking) in the samples after irradiation at relatively low temperature (<400 °C).<sup>101,103,113,133,134,142,151,160–162,166,167</sup> As the temperature increases to above 500–600 °C, microcracking is largely eliminated due to the increasing recombination of the defects and decreasing lattice expansion, as shown in Fig. 19. These results show that under these irradiation conditions, Ti<sub>3</sub>AlC<sub>2</sub> has a much higher crack density than Ti<sub>3</sub>SiC<sub>2</sub> after irradiation. This microcracking is proportional to the extent of unit cell parameter variation (the variation of the parameters is smallest in Ti<sub>3</sub>SiC<sub>2</sub>). The existence of impurity phases [such as TiC in Ti<sub>2</sub>AlC or (Zr<sub>0.5</sub>Ti<sub>0.5</sub>)<sub>2</sub>AlC in (Zr<sub>0.5</sub>Ti<sub>0.5</sub>)<sub>3</sub>AlC<sub>2</sub>] could cause interphase cracking under irradiation,<sup>151</sup> which is attributed to different swelling/expansion between different phases. The occurrence of microcracking induced by ion irradiation also leads to a degradation of strength and reduction of the elastic modulus.<sup>166</sup>

For the compounds that are prone to amorphization under irradiation at room temperature, such as Zr<sub>2</sub>AlC,<sup>140</sup> microcracking mechanisms may be distinct. This requires further investigation. It should be noted that the formation of microcracks strongly depends not only on the irradiation-induced damage level (dpa) but also on other irradiation conditions, such as ion energy.<sup>103</sup>

Defects formed in the MAX phases during irradiation serve as obstacles to dislocation motion and thus to deformation. Therefore, ion irradiation-induced hardening has been observed in these materials.<sup>129,134,168</sup> Hardness increases with irradiation fluence due to the accumulation of defects until it reaches a saturation value. Irradiation at high temperature results in a less pronounced increase in hardness, which is attributed to the recovery of the defects.

### B. Formation of helium bubbles

In fission reactors, nuclear fuels release high energy He particles via  $\alpha$  decay, leading to bombardment of nearby materials with He ions. In fusion reactors, transmutation nuclear reactions produce more He gas. As with other ion irradiation conditions, this He ion irradiation induces structural evolution (unit cell swelling and phase transformations) in the MAX phases.<sup>132,139</sup> Yet this irradiation is distinct in that it also generates bubbles once the concentration of

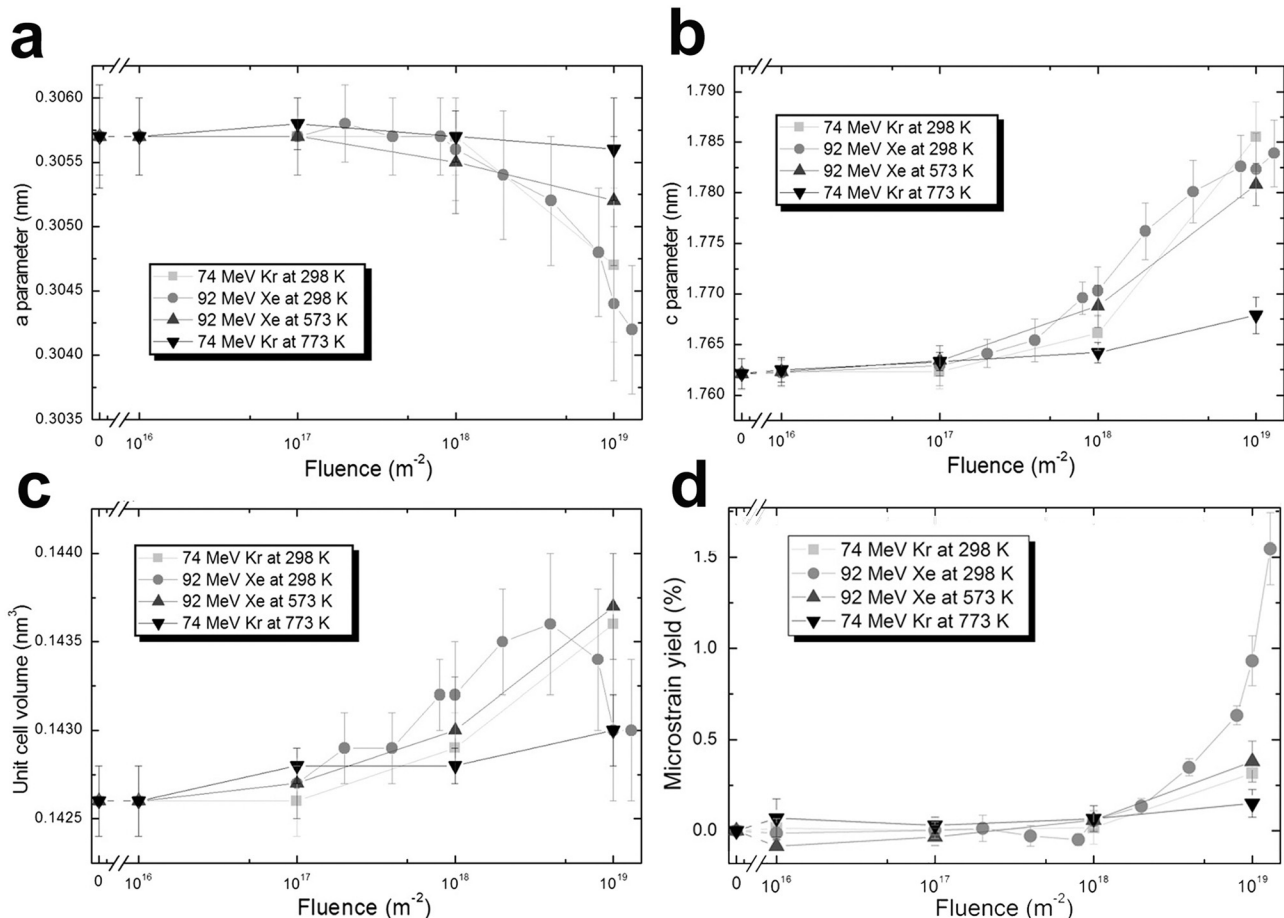


**FIG. 18.** Variation of the (a) a unit cell parameter, (b) c unit cell parameter, (c) unit cell volume, and (d) microstrain in  $\text{Ti}_3\text{SiC}_2$  under irradiation with 74 MeV Kr ions and 92 MeV Xe ions at room temperature, 300 °C, and 500 °C. Anisotropic change in the unit cell parameters is exhibited, as well as increasing volume swelling and microstrain with fluence. Reproduced with permission from Nappé *et al.*, J. Nucl. Mater. **409**, 53–61 (2011). Copyright 2011 Elsevier.

16 April 2024 01:14:22

implanted He reaches a critical value. This can promote void swelling, surface exfoliation, and degraded mechanical properties of materials.<sup>28</sup> He concentrations produced in current fission reactors are relatively low compared with those encountered in fusion reactors, where ceramics such as  $\text{Al}_2\text{O}_3$  and SiC exposed to 14 MeV fusion neutrons can accumulate He concentrations on the order of 60–150 atomic parts per million (appm) for radiation doses of one dpa.<sup>169</sup> This corresponds to He concentrations greater than 1.2–3 at. % for materials in the first wall region of the fusion reactors, where damage levels reach  $\sim 200$  dpa.

Figures 20(a)–20(c) show He bubbles formed in  $\text{Ti}_3\text{AlC}_2$  under 500 keV He irradiation to various fluences at room temperature. At a fluence of  $5 \times 10^{16} \text{ cm}^{-2}$ , isolated spherical helium bubbles with average radii of  $\sim 0.6 \text{ nm}$  are observed, with a corresponding He concentration of 3.2 at. %. As the fluence increases, these bubbles slightly grow by absorbing the adjacent He atoms [Fig. 20(b)], then coalesce into larger, string-shaped bubbles [Fig. 20(c)]. Under He irradiation at high temperature, the mobility of the He atoms increases, leading to the aggregation of the He atoms and the formation of larger He

bubbles with larger size, as shown in Fig. 20(d).<sup>137</sup> Bubble/cavity formation has been shown to be preferentially associated with specific low-index planes, including the basal plane of the hexagonal structure, at elevated temperatures.<sup>162</sup> Similar He bubbles were also observed in irradiated samples annealed at elevated temperature, as shown in Fig. 20(e).<sup>136</sup> The presence of grain boundaries and interfaces enhances the aggregation of helium bubbles, as observed in, for example,  $\text{V}_2\text{AlC}/\text{Zr}$  interfaces [Fig. 20(f)].<sup>170</sup> This is attributed to the presence of defects (misfit dislocations) along the boundary or interface, where bubbles or cavities preferentially initiate. The formation of He bubbles and cavities in the MAX phases can result in severe subsurface blistering, or even surface exfoliation if the He concentration is greater than around 15 at. %, as shown in Fig. 20(g).<sup>100</sup>

*Ab initio* calculations show that implanted helium in  $\text{Ti}_3\text{AlC}_2$ <sup>171</sup> and  $\text{Cr}_2\text{AlC}$ <sup>172</sup> preferentially occupies interstitial or substitutional sites in the Al layer. Trapped He atoms in the Al layer can promote further vacancy formation and He bubbles trapped by Al vacancies tend to grow in the Al plane of  $\text{Ti}_3\text{AlC}_2$ . The migration energy barrier of He diffusion in  $\text{Ti}_3\text{AlC}_2$  along the basal plane is one order of magnitude

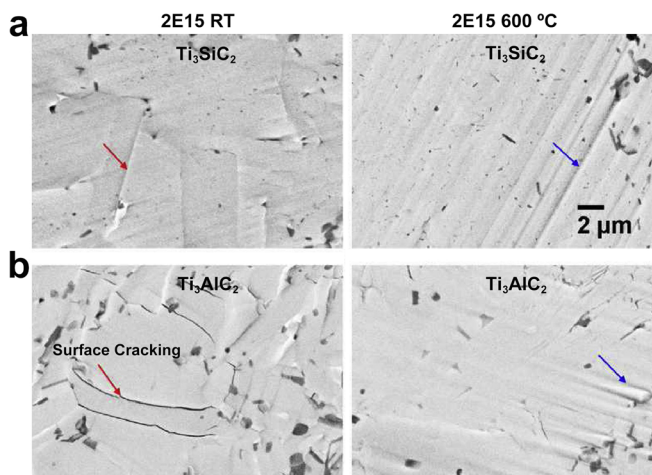


**FIG. 19.** SEM images of (a)  $\text{Ti}_3\text{SiC}_2$ , (b)  $\text{Ti}_3\text{AlC}_2$  irradiated to the fluence of  $2 \times 10^{15} \text{ cm}^{-2}$  at RT and  $600^\circ\text{C}$ , showing that surface cracking  $\text{Ti}_3\text{AlC}_2$  has a much higher crack density than  $\text{Ti}_3\text{SiC}_2$  after irradiation at room temperature. Reproduced with permission from Huang *et al.*, J. Nucl. Mater. **465**, 640–647 (2015). Copyright 2015 Elsevier.

smaller than that along the *c*-axis.<sup>173</sup> These results indicate that implanted He atoms will tend to easily migrate along the basal plane and therefore might be released from the surface of materials through grain boundaries.

### C. Electrical and thermal properties

Barssoum has shown that in most MAX phases, thermal conductivity depends strongly on electron transport due to the metallic characteristics of these materials. For example, >90% of the conductivity in  $\text{Ti}_3\text{SiC}_2$  is electronic thermal conductivity due to its suppressed phonon conductivity.<sup>13</sup> Therefore, electrical resistivity is an important index that can partially represent the thermal conductivity of these materials.

Energetic ions' penetration depths in materials are generally less than several tens of micrometers, making it difficult to measure the effects of irradiation on electrical resistivity. Typically, the collision of high-energy neutrons with lattice atoms creates point defects, increase the dangling bond density, and result in an increase in resistivity.<sup>174</sup>

Tallman *et al.*<sup>112,141,142</sup> studied the effects of neutron irradiation on electrical and thermal properties of several representative MAX phases:  $\text{Ti}_3\text{AlC}_2$ ,  $\text{Ti}_3\text{SiC}_2$ ,  $\text{Ti}_2\text{AlC}$ , and  $\text{Ti}_2\text{AlN}$ , as shown in Fig. 21. Their results show that the resistivity increases with irradiation fluence, which is attributed to the production of point defects that can efficiently scatter charge carrier. Among these MAX phases studied, only  $\text{Ti}_3\text{SiC}_2$  appears to approach a saturation in resistivity after irradiation to 0.1 dpa. It should be noted that grain size dramatically influences the relationship between irradiation and resistivity due to the activity of grain boundaries as defect sinks. The resistivity of fine-grained (FG)  $\text{Ti}_3\text{SiC}_2$  after irradiation ( $1.43 \mu\Omega\cdot\text{m}$ ) is roughly half that of the coarse-grained (CG)  $\text{Ti}_3\text{SiC}_2$  ( $2.82 \mu\Omega\cdot\text{m}$ ), which is attributed to the former's higher density of grain boundaries than the latter. Additionally, as temperature increases, the irradiation-induced change of resistivity decreases because of the annihilation of the point defects

and formation of larger defects (dislocation loops) or defect networks that are more coherent with the lattice and therefore scatter electrons less effectively.

Table II summarizes the radiation effects in most of the researched MAX phases under various kinds of neutron and ion irradiation over a wide range of temperature.

### VI. SUMMARY AND FUTURE PERSPECTIVES

In the past decade, radiation effects on MAX phases have been widely studied. In this review, we systematically assessed research results on irradiation-induced defect formation and migration, structural evolution, and the changes in macroscopic properties, as well as the role of the compositional factors on the radiation response. The irradiation-induced crystalline-to-crystalline transformation entails disordering to an fcc solid solution. Additionally, bond strength serves as a powerful determinant of the susceptibility of MAX phases to irradiation-induced phase transformation. However, considering the great chemical diversity of the MAX phase family (over 155 compositions) and diversity in the conditions of irradiation (i.e., particle mass and energy), far more research is needed to comprehensively explain and predict the behavior of MAX phases under irradiation. Below, we address several key facets of this research area that require further study.

#### A. Systematic, application-oriented research design

Even for the most studied MAX phases,  $\text{Ti}_3\text{AlC}_2$  and  $\text{Ti}_3\text{SiC}_2$ , the data available in the literature are insufficient for meaningful application to nuclear systems design. To date, approximately 60% of experimental studies of radiation effects on MAX phases were carried out only at room temperature. While these studies can help to explain the fundamental mechanism of structural evolution in MAX phases, these compounds, as potential candidate materials in nuclear reactors, must be further evaluated under the high-temperature conditions typical of reactor component operation. For example, as Tunes *et al.*<sup>122</sup> suggested, if the aim is to use the MAX phases in next generation fission reactors, especially those operated at relatively high temperatures (high-temperature gas-cooled reactors and molten salt reactors), they must exhibit structural stability at high temperatures up to  $1000^\circ\text{C}$ . Furthermore, reactor components may be subjected to damage levels up to 200 dpa, while most of the current research is limited to relatively low radiation doses. To address this gap, MAX phases should be studied under irradiation at high temperatures and high radiation doses, simulating reactor component operating environments.

In addition, macroscopic properties are critically important to MAX phases performance in engineering applications. Thus far, the structural characterization of radiation effects is insufficient for this application. Changes in physical properties, specifically mechanical thermal, and chemical properties, need to be further explored. Corrosion is another important aspect in nuclear materials and irradiation can enhance stress corrosion cracking that dramatically influences materials' properties.<sup>175</sup> Therefore, the corrosion resistance of MAX phases should be studied after irradiation.

For theoretical and computational work, almost all studies to date have focused on the behavior and properties at equilibrium for hexagonal MAX phases, including their electron density distribution, density of state, and defect behavior. But MAX phases used in nuclear applications are unlikely to fully retain this initial structure. Based on

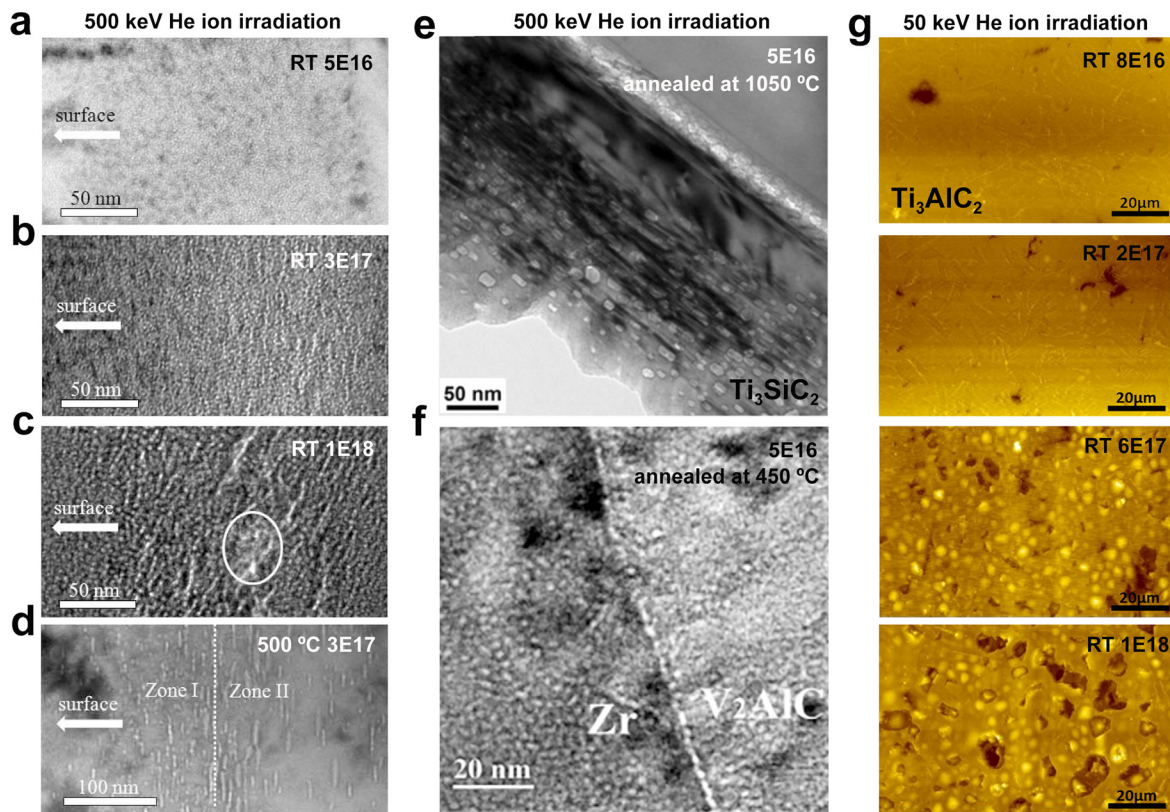


**FIG. 20.** Bright-field (BF) cross-sectional TEM images of (a) pristine  $\text{Ti}_3\text{AlC}_2$  and samples irradiated at room temperature to fluences of (b)  $3 \times 10^{17} \text{ cm}^{-2}$  and (c)  $1 \times 10^{18} \text{ cm}^{-2}$  as well as (d) a sample irradiated to a fluence of  $3 \times 10^{17} \text{ cm}^{-2}$  at  $500^\circ\text{C}$ . These micrographs show the evolution of He bubbles with increasing fluence and temperature. Reproduced with permission from Song *et al.*, Nucl. Instrum. Methods Phys. Res., Sect. B **326**, 332–336 (2014). Copyright 2014 Elsevier. (e) BF TEM image of  $\text{Ti}_3\text{AlC}_2$  irradiated to a fluence of  $5 \times 10^{16} \text{ cm}^{-2}$  annealed at  $1050^\circ\text{C}$ , indicating the accumulation of implanted He atoms and the formation of He bubbles. Reproduced with permission from Zhang *et al.*, J. Eur. Ceram. Soc. **38**, 1253–1264 (2018). Copyright 2017 Elsevier. (f) BF TEM image of an interface in  $\text{V}_2\text{AlC}/\text{Zr}$  irradiated to a fluence of  $5 \times 10^{16} \text{ cm}^{-2}$ , then annealed at  $450^\circ\text{C}$  for 5 h, indicating that He bubbles preferentially initiate and congregate along the interface. Reproduced with permission from Wang *et al.*, Scr. Mater. **137**, 13–17 (2017). Copyright 2017 Elsevier. (g) Surface morphology of  $\text{Ti}_3\text{AlC}_2$  irradiated to various fluences at room temperature, showing surface blistering and exfoliation. Reproduced with permission from Wang *et al.*, J. Nucl. Mater. **440**, 606–611 (2013). Copyright 2013 Elsevier.

16 April 2024 01:28:24

the irradiation-induced phase transformations discussed above, there exist several additional phases, such as the  $\gamma$ ,  $\delta$ , and fcc phases, that may be relevant to material performance. The structures of these phases also depend on the initial composition. For example, the  $\gamma\text{-Ti}_2\text{AlC}$  phase possess a structure distinct from that of the  $\gamma\text{-Cr}_2\text{AlC}$  phase. Current theoretical and computational work does not sufficiently evaluate and explain the radiation responses, defect behaviors, and properties of these irradiation-induced phases. Therefore, future research should focus on these additional phases, particularly the fcc solid solutions that are most commonly produced in response to irradiation.

## B. Expanded compositional space

Up to now, radiation effects have been studied in fewer than 20 MAX phases. Lack of data on the more than 100 other MAX phases significantly limits the development of these materials. Therefore, it is critical to expand the composition space explored in MAX phase radiation effects studies. As mentioned above, these unaddressed phases

include other conventional MAX phases, higher order  $M_{n+1}\text{AX}_n$  phases ( $n = 4, 5, 6$ ), ordered  $(M, M')_{n+1}\text{AX}_n$  phases, random solid solution phases, hybrid MAX phases, and other derivative phases with distinct structures. Study of these materials could further verify the mechanisms of structural evolution and the roles of various compositional factors in their behavior under irradiation, allowing for better prediction and optimization of MAX phase radiation tolerance. In addition, two new varieties of MAX phase materials have recently attracted a large amount of interest with respect to their potential nuclear applications: high-entropy MAX phases and RE-i-MAX phases.

During the past years, high-entropy alloys<sup>180</sup> and high-entropy ceramics (including carbides, borides, oxides, nitrides, silicides, and oxycarbonitrides)<sup>181,182</sup> have received increasing attention in various research fields due to their unique structures and properties. Their alloying effects can change the behavior of point defects, further influencing the structural stability, electronic structures, and diffusion barriers for defects in MAX phases.<sup>183</sup> Even though the idea of synthesizing high-entropy MAX phases is relatively simple, only limited

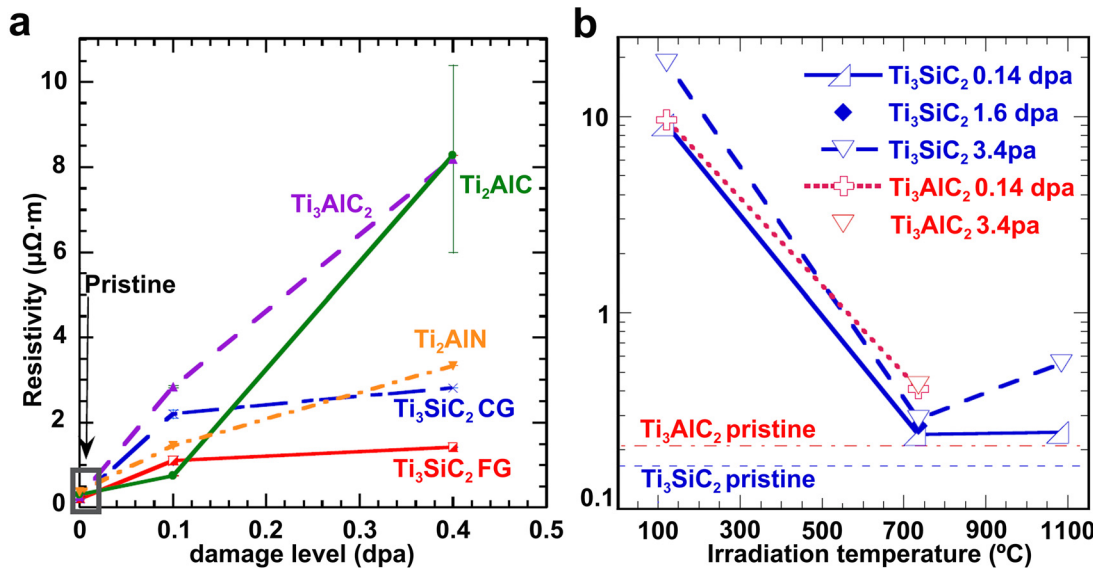


**FIG. 21.** (a) Resistivity of various MAX phases after neutron irradiation at 360 °C to a damage level of 0.1 dpa. (b) Resistivity of  $Ti_3AlC_2$  and  $Ti_3SiC_2$  after neutron irradiation as a function of temperature. Reproduced with permission from Tallman *et al.*, J. Nucl. Mater. **468**, 194–206 (2016). Copyright 2015 Elsevier. Reproduced with permission from Tallman *et al.*, J. Nucl. Mater. **484**, 120–134 (2017). Copyright 2016 Elsevier.

research has been published on these materials in the last few years.<sup>184,185</sup> Their precise performance under irradiation conditions remains unknown. Based on study of high-entropy alloys,<sup>186</sup> it is suspected that the radiation tolerance of high-entropy MAX phases might be superior to that of conventional MAX phases.

The recent discovery of quaternary MAX phases, such as  $(M, M')_{n+1}AX_n$ , with chemical in-plane order facilitates the incorporation of nontraditional MAX phase elements, including rare-earth elements. Recently, novel rare-earth containing in-plane-ordered MAX phases, referred to as RE-i-MAX phases, with the general formula  $(M_{2/3}RE_{1/3})_2AC$  (RE = Nd, Sm, Gd, Tb, Dy, Ho, Er, Tm, and Lu) have been successfully synthesized.<sup>187–190</sup> This suggests that it may also be possible to incorporate actinide elements, such as uranium and plutonium, into MAX phases, raising the possibility of their use in nuclear fuels or waste forms.<sup>191</sup> This idea originates from the application of complex oxides (such as  $A_2B_2O_7$  with a pyrochlore structure) for nuclear waste disposal.<sup>192</sup> One critical factor in the design of nuclear waste form materials is their susceptibility to irradiation-induced damage. However, both experimental and computational results have shown that some complex oxides readily become amorphous under irradiation, while most of the MAX phases studied to date exhibit excellent resistance to irradiation-induced amorphization. Therefore, RE-i-MAX phases deserve further study as candidate materials for the immobilization and disposal of nuclear waste.

### C. MAX phase thin films and composites

Almost all the MAX phase materials used in radiation damage studies to date have been polycrystalline bulk materials. However, MAX phases are often proposed as components of composite materials, particularly in nuclear applications. One commonly proposed application of MAX phases is as coatings on zirconium alloy nuclear fuel cladding components that serve to contain nuclear fuel in nuclear

reactors, isolating the fuel from the reactor coolant. Due to differences in synthesis and the existence of a substrate-coating interface, the properties of bulk MAX phases might be different from those of MAX phase thin films.<sup>10</sup> The response of MAX phase thin films<sup>128,193</sup> and Zircaloy<sup>194</sup> to irradiation has been studied separately, but Zircaloy materials coated with MAX phase films have not been adequately characterized (particularly with respect to their behavior at the interface). Interactions between the coating MAX phases and Zircaloy fuel cladding are expected to occur at the high operational temperatures in nuclear reactors, leading to the formation of intermetallic phases.<sup>167,168</sup> Therefore, it is critical to study structural evolution and defect accumulation, particularly along the interface, as well as the mechanical properties of these MAX phase coated materials under irradiation at elevated temperatures.

In addition to coatings and thin films, MAX phases have been used as composite inclusions in SiC matrices to improve their properties and machinability.<sup>195–199</sup> For example, Katoh *et al.* studied the shear strength in  $Ti_3SiC_2$  chemical vapor deposition (CVD) SiC joints after irradiation.<sup>200</sup> However, more information on the chemical stability, structural evolution, and degradation of properties of these materials under irradiation is needed. Specifically, the occurrence of different irradiation-induced volumetric swelling rates between the MAX phases and SiC matrix, along with interface reactions and thermal mismatches, could lead to severe cracking in these composites.

### D. MAX-derivative phases

Following the discovery of the unique physical properties of graphene, two dimensional (2D) materials have been widely researched, including MAX phase derivatives: MXenes.<sup>117,118,201–203</sup> These materials are produced by etching A layers from MAX phase in concentrated hydrofluoric acid and exhibit properties that differ from those of their 3D counterparts. Due to their unique 2D structures and rare

**TABLE II.** Summary of prior research on radiation effects in representative MAX phases

Irradiation parameters	Irradiation T (K)	Compositions	Radiation effects
1 MeV Au ions	RT	Ti <sub>3</sub> AlC <sub>2</sub> , Ti <sub>3</sub> SiC <sub>2</sub> , Ti <sub>2</sub> AlC, V <sub>2</sub> AlC, Cr <sub>2</sub> AlC, Ti <sub>2</sub> AlN, Ti <sub>4</sub> AlN <sub>3</sub> <sup>47,104–106,108,109</sup>	Formation of antisite defects at low fluences; Transformation to fcc (except for Cr <sub>2</sub> AlC which is amorphized); Resistance to phase transformation: Ti <sub>3</sub> AlC <sub>2</sub> > Ti <sub>3</sub> SiC <sub>2</sub> , Ti <sub>3</sub> AlC <sub>2</sub> > Ti <sub>2</sub> AlC, Ti <sub>4</sub> AlN <sub>3</sub> > Ti <sub>2</sub> AlN Ti <sub>2</sub> AlC > V <sub>2</sub> AlC > Cr <sub>2</sub> AlC Ti <sub>2</sub> AlC > Ti <sub>2</sub> AlN
4 MeV Au ion	RT	Ti <sub>3</sub> SiC <sub>2</sub> <sup>84,175</sup>	Formation of “hills” on the surface
240 keV Ar ion	RT	Ti <sub>3</sub> AlC <sub>2</sub> <sup>123</sup>	Transformation to fcc [Ti <sub>3</sub> (Al,C <sub>2</sub> ) solid solution]
50 keV –500 keV He ion	RT 773	Ti <sub>3</sub> AlC <sub>2</sub> <sup>100,102,107,132,137,138</sup> Ti <sub>3</sub> SiC <sub>2</sub> <sup>136,139</sup> V <sub>2</sub> AlC/Zr <sup>170</sup>	Transformation to fcc; Formation of He bubbles and “faulting zone;” Surface exfoliating at high irradiation fluences; Aggregation of He bubbles along the V <sub>2</sub> AlC/Zr interfaces
2 MeV I ion, 700 keV C ion, 1.1 MeV C ion	RT- 1123	Ti <sub>3</sub> SiC <sub>2</sub> <sup>98,99</sup> Ti <sub>2</sub> AlC <sup>134</sup> Ti <sub>3</sub> AlC <sub>2</sub> <sup>110</sup>	Transformation to fcc; Structure partially recovered after annealing; Hexagonal structure retained at high T
100 keV Kr ion	RT	(Ti,Al)N/Ti <sub>2</sub> AlN <sub>x</sub> <sup>22</sup>	Not sensitive to amorphization
1 MeV Kr ion	RT-1073	Ti <sub>2</sub> AlC <sup>143</sup>	Formation of dislocation loops and stacking faults on the basal plane
74 MeV Kr ion	RT, 573, 773	Ti <sub>3</sub> Si <sub>0.90</sub> Al <sub>0.10</sub> C <sub>2</sub> <sup>24,176</sup> Ti <sub>3</sub> SiC <sub>2</sub> <sup>124</sup>	Increase of hardness with irradiation fluence; Structure recovered via post-irradiation annealing; Change of unit cell parameters after irradiation: contraction along <i>a</i> axis, expansion along <i>c</i> axis
5.8 MeV Ni	673, 973	Ti <sub>3</sub> AlC <sub>2</sub> , Ti <sub>3</sub> SiC <sub>2</sub> , Ti <sub>2</sub> AlC <sup>133</sup>	Transformation to fcc; Surface cracking in Ti <sub>3</sub> AlC <sub>2</sub> and Ti <sub>2</sub> AlC
340 keV –7 MeV Xe ion	RT	Ti <sub>3</sub> AlC <sub>2</sub> , Ti <sub>3</sub> SiC <sub>2</sub> <sup>103,149</sup> Cr <sub>2</sub> AlC, Cr <sub>2</sub> GeC <sup>177</sup>	Resistance to irradiation-induced amorphization: Ti <sub>3</sub> AlC <sub>2</sub> > Ti <sub>3</sub> SiC <sub>2</sub> , Cr <sub>2</sub> AlC > Cr <sub>2</sub> GeC
~90 MeV Xe ion	RT, 573, 773	Ti <sub>3</sub> SiC <sub>2</sub> , <sup>23</sup> (Ti,Zr) <sub>3</sub> (Si,Al)C <sub>2</sub> , <sup>178</sup> Ti <sub>3</sub> Si <sub>0.90</sub> Al <sub>0.10</sub> C <sub>2</sub> , <sup>24</sup>	Initial structure disturbed with no amorphization; Phase transformation ( $\alpha$ to $\beta$ ); Increase of hardness with irradiation fluence; Smaller change of unit cell parameters at higher T
9 MeV Ti ion, 14 MeV Cl, 17 MeV Pt	RT	Ti <sub>3</sub> SiC <sub>2</sub> <sup>111,135</sup>	Transformation to fcc; At high electronic stopping (high ion energy), the phase transformation is fully suppressed and lattice strain is maximized.
2 MeV proton ion	RT-873	Zr <sub>3</sub> AlC <sub>2</sub> , Ti <sub>3</sub> AlC <sub>2</sub> , Ti <sub>3</sub> SiC <sub>2</sub> , Nb <sub>4</sub> AlC <sub>3</sub> , (Zr,Ti) <sub>3</sub> AlC <sub>2</sub> 113 <sup>113,150</sup>	Surface cracking; surface exfoliation; Change of unit cell parameters after irradiation: contraction along <i>a</i> axis, expansion along <i>c</i> axis
Neutron	394–1358	Ti <sub>3</sub> AlC <sub>2</sub> , Ti <sub>3</sub> SiC <sub>2</sub> , Ti <sub>2</sub> AlC, Ti <sub>2</sub> AlN, Ti <sub>3</sub> AlC <sub>2</sub> -Ti <sub>5</sub> Al <sub>2</sub> C <sub>3</sub> , <sup>112,141,142,161,166</sup>	Transformation to fcc; Formation of dislocation loops and stacking faults on the basal plane; Increase of RT resistivity after irradiation; Decrease of RT strength after irradiation

combination of good electronic conductivity and hydrophilicity, MXenes exhibit a broad range of potential applications, such as materials for electrochemical energy storage.<sup>204</sup> The surface terminated groups of MXenes also dramatically influence their crystal and electronic structure, chemical bonding characteristics, and elastic properties.<sup>205</sup> Although MXenes have not been proposed for use in nuclear energy systems, these materials may have unique responses to irradiation that could elucidate the fundamental irradiation-induced behavior of MAX phase-like materials. Furthermore, ion beam irradiation serves not only as a means of simulating nuclear energy system operating conditions but also as a means of tailoring the structures and properties of materials.<sup>206–208</sup> Therefore, ion beam processing studies of the MXenes may prove a fruitful area of research.

## E. MAB phases

Recently, researchers have reported another class of layered ternary ceramics, known as MAB phases (where M is transition metal, A is aluminum and B is boron). This class of materials includes two distinct stoichiometries: MAB (space group *Cmcm*) and  $M_2AB_2$  (space group *Cmmm*). The structures of these materials are similar to those of the MAX phases, with the transition metal carbides or borides interleaved by A layers. Many MAB phases have been successfully synthesized (M = Mo, W, Cr, Mn, Fe, and Ru)<sup>209</sup> and considered for use in the nuclear energy applications, for example, neutron shielding in fission and fusion reactors as well as neutron absorbers for the storage of spent nuclear fuel.<sup>210</sup> More recently, Zhang *et al.*<sup>211</sup> studied the defect behavior and radiation tolerance of two typical MAB phases, i.e., MoAlB and  $Fe_2AlB_2$ . The results show that  $Fe_2AlB_2$  is highly tolerant to radiation-induced amorphization and no radiation-induced cracking occurred in either materials. However, more information on the structural evolution and properties of these MAB phases under irradiation is needed. As work on MAX phases continues, exploration of MAB phases and related systems should proceed in parallel to further expand the composition space available for study.

## ACKNOWLEDGMENTS

This work was supported by the National Magnetic Confinement Fusion Energy Research Project of China (No. 2015GB113000), the National Natural Science Foundation of China (Nos. 11935004 and 11675005), Peking University Project for Establishment of First-class Universities and Disciplines of the World and funding from the U.S. Department of Energy, National Nuclear Security Administration, Office of Defense Nuclear Nonproliferation Research and Development under Contract No. DE-AC02-76SF00515. Part of this work was performed at the Stanford Nano Shared Facilities (SNSF), supported by the National Science Foundation under Award No. ECCS-1542152. The authors thank the staff of Beijing Synchrotron Radiation Facility (BSRF) for the GIXRD measurements.

## DATA AVAILABILITY

The data that support the findings of this study are available from the corresponding authors upon reasonable request.

## REFERENCES

- <sup>1</sup>W. Jeitschko, H. Nowotny, and F. Benesovsky, *Monatsh. Chem. Verw. Teile anderer Wiss.* **94**, 1198 (1963).
- <sup>2</sup>W. Jeitschko, H. Nowotny, and F. Benesovsky, *Monatsh. Chem. Verw. Teile anderer Wiss.* **95**, 431 (1964).
- <sup>3</sup>W. Jeitschko, H. T. Nowotny, and F. Benesovsky, *J. Less Common Met.* **7**, 133 (1964).
- <sup>4</sup>W. Jeitschko and H. Nowotny, *Monatsh. Chem.* **98**, 329 (1967).
- <sup>5</sup>V. H. Nowotny, *Prog. Solid State Chem.* **5**, 27 (1971).
- <sup>6</sup>M. W. Barsoum and T. El-Raghy, *Ti<sub>3</sub>SiC<sub>2</sub>* **79**, 1953 (1996).
- <sup>7</sup>M. W. Barsoum, *Prog. Solid State Chem.* **28**, 201 (2000).
- <sup>8</sup>M. W. Barsoum and T. El-Raghy, *Am. Sci.* **89**, 334 (2001).
- <sup>9</sup>J. Wang and Y. Zhou, *Annu. Rev. Mater. Res.* **39**, 415 (2009).
- <sup>10</sup>P. Eklund, M. Beckers, U. Jansson, H. Höglberg, and L. Hultman, *Thin Solid Films* **518**, 1851 (2010).
- <sup>11</sup>X. Wang and Y. Zhou, *J. Mater. Sci. Technol.* **26**, 385 (2010).
- <sup>12</sup>Z. M. Sun, *Int. Mater. Rev.* **56**, 143 (2011).
- <sup>13</sup>M. W. Barsoum, *MAX Phases: Properties of Machinable Ternary Carbides and Nitrides* (John Wiley and Sons, 2013).
- <sup>14</sup>I.-M. Low, *MAX Phases and Ultra-High Temperature Ceramics for Extreme Environments* (IGI Global, 2013).
- <sup>15</sup>M. Radovic and M. W. Barsoum, *Am. Ceram. Soc. Bull.* **92**, 20 (2013).
- <sup>16</sup>H. O. Pierson, *Handbook of Refractory Carbides and Nitrides: Properties, Characteristics, Processing and Apps* (William Andrew, 1996).
- <sup>17</sup>S. Gupta, D. Filimonov, V. Zaitsev, T. Palanisamy, T. El-Raghy, and M. W. Barsoum, *Wear* **267**, 1490 (2009).
- <sup>18</sup>M. Sundberg, G. Malmqvist, A. Magnusson, and T. El-Raghy, *Ceram. Int.* **30**, 1899 (2004).
- <sup>19</sup>D. E. Hajas, M. to Baben, B. Hallstedt, R. Iskandar, J. Mayer, and J. M. Schneider, *Surf. Coat. Technol.* **206**, 591 (2011).
- <sup>20</sup>E. N. Hoffman, D. W. Vinson, R. L. Sindelar, D. J. Tallman, G. Kohse, and M. W. Barsoum, *Nucl. Eng. Des.* **244**, 17 (2012).
- <sup>21</sup>B. Garcia-Diaz, L. Olson, C. Verst, R. Sindelar, E. Hoffman, B. Hauch, B. Maier, and K. Sridharan, *Trans. Am. Nucl. Soc.* **110**, 994 (2014).
- <sup>22</sup>M. Bugnet, T. Cabioch, V. Mauchamp, P. Guérin, M. Marteau, and M. Jaouen, *J. Mater. Sci.* **45**, 5547 (2010).
- <sup>23</sup>M. Le Flem, X. Liu, S. Doriot, T. Cozzika, and I. Monnet, *Int. J. Appl. Ceram. Technol.* **7**, 766 (2010).
- <sup>24</sup>X. Liu, M. Le Flem, J.-L. Béchade, F. Onimus, T. Cozzika, and I. Monnet, *Nucl. Instrum. Methods Phys. Res., Sect. B* **268**, 506 (2010).
- <sup>25</sup>J. Xie, X. Wang, A. Li, F. Li, and Y. Zhou, *Corros. Sci.* **60**, 129 (2012).
- <sup>26</sup>L. A. Barnes, N. L. Dietz Rago, and L. Leibowitz, *J. Nucl. Mater.* **373**, 424 (2008).
- <sup>27</sup>S. J. Zinkle and G. S. Was, *Acta Mater.* **61**, 735 (2013).
- <sup>28</sup>S. J. Zinkle, *Nucl. Instrum. Methods Phys. Res., Sect. B* **286**, 4 (2012).
- <sup>29</sup>SME Presidential Task Force on Response to Japan Nuclear Power Plant Events, *Mech. Eng.* **134**, 46 (2012).
- <sup>30</sup>S. J. Zinkle, K. A. Terrani, J. C. Gehin, L. J. Ott, and L. L. Snead, *J. Nucl. Mater.* **448**, 374 (2014).
- <sup>31</sup>K. A. Terrani, *J. Nucl. Mater.* **501**, 13 (2018).
- <sup>32</sup>B. A. Pint, K. A. Terrani, Y. Yamamoto, and L. L. Snead, *Metall. Mater. Trans. E* **2**, 190 (2015).
- <sup>33</sup>B. R. Maier, B. L. Garcia-Diaz, B. Hauch, L. C. Olson, R. L. Sindelar, and K. Sridharan, *J. Nucl. Mater.* **466**, 712 (2015).
- <sup>34</sup>M. Sokol, V. Natu, S. Kota, and M. W. Barsoum, *Trends Chem.* **1**, 210 (2019).
- <sup>35</sup>W. B. Zhou, B. C. Mei, J. Q. Zhu, and X. L. Hong, *Mater. Lett.* **59**, 131 (2005).
- <sup>36</sup>M. Pietzka and J. Schuster, *J. Phase Equilib.* **15**, 392 (1994).
- <sup>37</sup>C. Rawn, M. Barsoum, T. El-Raghy, A. Procipio, C. Hoffmann, and C. Hubbard, *Mater. Res. Bull.* **35**, 1785 (2000).
- <sup>38</sup>L. Farber, M. W. Barsoum, A. Zavaliongos, T. El-Raghy, and I. Levin, *J. Am. Ceram. Soc.* **81**, 1677 (1998).
- <sup>39</sup>X. H. Deng, B. B. Fan, and W. Lu, *Solid State Commun.* **149**, 441 (2009).
- <sup>40</sup>X. He, Y. Bai, C. Zhu, and M. W. Barsoum, *Acta Mater.* **59**, 5523 (2011).
- <sup>41</sup>C. Hu, Z. Lin, L. He, Y. Bao, J. Wang, M. Li, and Y. Zhou, *J. Am. Ceram. Soc.* **90**, 2542 (2007).
- <sup>42</sup>Y. Zhou, F. Meng, and J. Zhang, *J. Am. Ceram. Soc.* **91**, 1357 (2008).
- <sup>43</sup>A. Mockute, M. Dahlqvist, J. Emmerlich, L. Hultman, J. M. Schneider, P. O. Å. Persson, and J. Rosen, *Phys. Rev. B* **87**, 094113 (2013).
- <sup>44</sup>M. Higashi, S. Momono, K. Kishida, N. L. Okamoto, and H. Inui, *Acta Mater.* **161**, 161 (2018).

- <sup>45</sup>Z. Lin, M. Zhuo, Y. Zhou, M. Li, and J. Wang, *J. Appl. Phys.* **99**, 076109 (2006).
- <sup>46</sup>Z. Lin, M. Li, and Y. Zhou, *J. Mater. Sci. Technol.* **23**, 145 (2007).
- <sup>47</sup>C. Wang, T. Yang, C. L. Tracy, C. Lu, H. Zhang, Y.-J. Hu, L. Wang, L. Qi, L. Gu, Q. Huang, J. Zhang, J. Wang, J. Xue, R. C. Ewing, and Y. Wang, *Nat. Commun.* **10**, 622 (2019).
- <sup>48</sup>Z. Wang, M. Saito, K. P. McKenna, L. Gu, S. Tsukimoto, A. L. Shluger, and Y. Ikuhara, *Nature* **479**, 380 (2011).
- <sup>49</sup>P. E. Pearce, A. J. Perez, G. Rousse, M. Saubanère, D. Batuk, D. Foix, E. McCalla, A. M. Abakumov, G. Van Tendeloo, and M.-L. Doublet, *Nat. Mater.* **16**, 580 (2017).
- <sup>50</sup>Z. J. Lin, M. J. Zhuo, Y. C. Zhou, M. S. Li, and J. Y. Wang, *J. Mater. Res.* **21**, 2587 (2006).
- <sup>51</sup>Z. Liu, E. Wu, J. Wang, Y. Qian, H. Xiang, X. Li, Q. Jin, G. Sun, X. Chen, J. Wang, and M. Li, *Acta Mater.* **73**, 186 (2014).
- <sup>52</sup>J. Zhang, B. Liu, J. Y. Wang, and Y. C. Zhou, *J. Mater. Res.* **24**, 39 (2009).
- <sup>53</sup>J. P. Palmquist, S. Li, P. Persson, J. Emmerlich, O. Wilhelmsson, H. Höglberg, M. Katsnelson, B. Johansson, R. Ahuja, O. Eriksson, L. Hultman, and U. Jansson, *Phys. Rev. B* **70**, 165401 (2004).
- <sup>54</sup>Z. Lin, M. Zhuo, Y. Zhou, M. Li, and J. Wang, *J. Am. Ceram. Soc.* **89**, 3765 (2006).
- <sup>55</sup>B. Anasori, M. Dahlqvist, J. Halim, E. J. Moon, J. Lu, B. C. Hosler, E. A. N. Caspi, S. J. May, L. Hultman, and P. Eklund, *J. Appl. Phys.* **118**, 094304 (2015).
- <sup>56</sup>Y. C. Zhou, J. X. Chen, and J. Y. Wang, *Acta Mater.* **54**, 1317 (2006).
- <sup>57</sup>W. Yu, V. Mauchamp, T. Cabioch, D. Magne, L. Gence, L. Piraux, V. Gauthier-Brunet, and S. Dubois, *Acta Mater.* **80**, 421 (2014).
- <sup>58</sup>K. Fukuda, S. Mori, and S. Hashimoto, *J. Am. Ceram. Soc.* **88**, 3528 (2005).
- <sup>59</sup>Z. J. Lin, L. F. He, M. S. Li, J. Y. Wang, and Y. C. Zhou, *J. Mater. Res.* **22**, 3058 (2011).
- <sup>60</sup>E. H. Lutz, M. V. Swain, and N. Claussen, *J. Am. Ceram. Soc.* **74**, 19 (1991).
- <sup>61</sup>X. Q. You, T. Z. Si, N. Liu, P. P. Ren, Y. D. Xu, and J. P. Feng, *Ceram. Int.* **31**, 33 (2005).
- <sup>62</sup>Y. W. Bao, X. H. Wang, H. B. Zhang, and Y. C. Zhou, *J. Eur. Ceram. Soc.* **25**, 3367 (2005).
- <sup>63</sup>A. Ganguly, T. Zhen, and M. W. Barsoum, *J. Alloys Compd.* **376**, 287 (2004).
- <sup>64</sup>X. Wang and Y. Zhou, *Acta Mater.* **50**, 3143 (2002).
- <sup>65</sup>Y. Zhou and Z. Sun, *Mater. Res. Innovations* **2**, 360 (1999).
- <sup>66</sup>M. Murabayashi, S. Tanaka, and Y. Takahashi, *J. Nucl. Sci. Technol.* **12**, 661 (1975).
- <sup>67</sup>M. W. Barsoum and M. Radovic, *Annu. Rev. Mater. Res.* **41**, 195 (2011).
- <sup>68</sup>Y. Zhou and X. Wang, *Mater. Res. Innovations* **5**, 87 (2001).
- <sup>69</sup>C. J. Gilbert, D. Bloyer, M. Barsoum, T. El-Raghy, A. Tomsia, and R. Ritchie, *Scr. Mater.* **42**, 761 (2000).
- <sup>70</sup>L. Farber and M. Barsoum, *J. Mater. Res.* **14**, 2560 (1999).
- <sup>71</sup>Y. Du, J. C. Schuster, H. J. Seifert, and F. Aldinger, *J. Am. Ceram. Soc.* **83**, 197 (2000).
- <sup>72</sup>W. K. Pang, I. M. Low, B. H. O'Connor, V. K. Peterson, A. J. Studer, and J. P. Palmquist, *J. Alloys Compd.* **509**, 172 (2011).
- <sup>73</sup>W.-K. Pang, I.-M. Low, and Z.-M. Sun, *J. Am. Ceram. Soc.* **93**, 2871 (2010).
- <sup>74</sup>M. Barsoum, T. El-Raghy, L. Farber, M. Amer, R. Christini, and A. Adams, *J. Electrochem. Soc.* **146**, 3919 (1999).
- <sup>75</sup>B. Manoun, S. K. Saxena, and M. W. Barsoum, *Appl. Phys. Lett.* **86**, 101906 (2005).
- <sup>76</sup>B. Manoun, R. P. Gulve, S. K. Saxena, S. Gupta, M. W. Barsoum, and C. S. Zha, *Phys. Rev. B* **73**, 024110 (2006).
- <sup>77</sup>B. Manoun, S. K. Saxena, T. El-Raghy, and M. W. Barsoum, *Appl. Phys. Lett.* **88**, 201902 (2006).
- <sup>78</sup>Z. Wang, C. S. Zha, and M. W. Barsoum, *Appl. Phys. Lett.* **85**, 3453 (2004).
- <sup>79</sup>Z. Feng, P. Ke, Q. Huang, and A. Wang, *Surf. Coat. Technol.* **272**, 380 (2015).
- <sup>80</sup>Y. Du, J.-X. Liu, Y. Gu, X.-G. Wang, F. Xu, and G.-J. Zhang, *Ceram. Int.* **43**, 7166 (2017).
- <sup>81</sup>G. Bentzel, M. Ghidiu, J. Griggs, A. Lang, and M. Barsoum, *Corros. Sci.* **111**, 568 (2016).
- <sup>82</sup>L. Li, G. Yu, and X. Zhou, *Nucl. Tech.* **37**, 6 (2014).
- <sup>83</sup>D. J. Tallman, B. Anasori, and M. W. Barsoum, *Mater. Res. Lett.* **1**, 115 (2013).
- <sup>84</sup>J. C. Nappé, P. Grosseau, F. Audubert, B. Guilhot, M. Beauvy, M. Benabdesselam, and I. Monnet, *J. Nucl. Mater.* **385**, 304 (2009).
- <sup>85</sup>G. Was, J. Busby, T. Allen, E. Kenik, A. Jansson, S. Bruemmer, J. Gan, A. Edwards, P. Scott, and P. Andresson, *J. Nucl. Mater.* **300**, 198 (2002).
- <sup>86</sup>T. Yang, C. A. Taylor, S. Kong, C. Wang, Y. Zhang, X. Huang, J. Xue, S. Yan, and Y. Wang, *J. Nucl. Mater.* **443**, 40 (2013).
- <sup>87</sup>J. F. Ziegler, M. D. Ziegler, and J. P. Biersack, *Nucl. Instrum. Methods Phys. Res., Sect. B* **268**, 1818 (2010).
- <sup>88</sup>K. Nordlund, S. J. Zinkle, A. E. Sand, F. Granberg, R. S. Averback, R. Stoller, T. Suzudo, L. Malerba, F. Banhart, W. J. Weber, F. Willaime, S. L. Dudarev, and D. Simeone, *Nat. Commun.* **9**, 1084 (2018).
- <sup>89</sup>H. Zhang, T. Hu, X. Wang, and Y. Zhou, *J. Mater. Sci. Technol.* **38**, 205 (2020).
- <sup>90</sup>S. C. Middleburgh, G. R. Lumpkin, D. Riley, and Y. Zhon, *J. Am. Ceram. Soc.* **96**, 308 (2013).
- <sup>91</sup>S. Zhao, J. Xue, Y. Wang, and Q. Huang, *J. Appl. Phys.* **115**, 023503 (2014).
- <sup>92</sup>S. Zhao, J. Xue, Y. Wang, and Q. Huang, *J. Phys. Chem. Solids* **75**, 384 (2014).
- <sup>93</sup>J. Xiao, T. Yang, C. Wang, J. Xue, and Y. Wang, *J. Am. Ceram. Soc.* **98**, 1323 (2015).
- <sup>94</sup>K. Sickafus, L. Minervini, R. Grimes, J. Valdez, M. Ishimaru, F. Li, K. McClellan, and T. Hartmann, *Science* **289**, 748 (2000).
- <sup>95</sup>R. C. Ewing, W. J. Weber, and J. Lian, *J. Appl. Phys.* **95**, 5949 (2004).
- <sup>96</sup>K. E. Sickafus, R. W. Grimes, J. A. Valdez, A. Cleave, M. Tang, M. Ishimaru, S. M. Corish, C. R. Stanek, and B. P. Uberuaga, *Nat. Mater.* **6**, 217 (2007).
- <sup>97</sup>G. Sattonnay, S. Moll, L. Thomé, C. Decorse, C. Legros, P. Simon, J. Jagielski, I. Jozwik, and I. Monnet, *J. Appl. Phys.* **108**, 103512 (2010).
- <sup>98</sup>L. Zhang, Q. Qi, L. Q. Shi, D. J. O'Connor, B. V. King, E. H. Kisi, and D. K. Venkatachalam, *Appl. Surf. Sci.* **258**, 6281 (2012).
- <sup>99</sup>C. Liu, L. Shi, Q. Qi, D. J. O'Connor, B. V. King, E. H. Kisi, X. B. Qing, and B. Y. Wang, *Nucl. Instrum. Methods Phys. Res., Sect. B* **307**, 536 (2013).
- <sup>100</sup>C. Wang, T. Yang, S. Kong, J. Xiao, J. Xue, Q. Wang, C. Hu, Q. Huang, and Y. Wang, *J. Nucl. Mater.* **440**, 606 (2013).
- <sup>101</sup>Q. Qi, G. J. Cheng, L. Q. Shi, D. J. O'Connor, B. V. King, and E. H. Kisi, *Acta Mater.* **66**, 317 (2014).
- <sup>102</sup>T. Yang, C. Wang, C. A. Taylor, X. Huang, Q. Huang, F. Li, L. Shen, X. Zhou, J. Xue, S. Yan, and Y. Wang, *Acta Mater.* **65**, 351 (2014).
- <sup>103</sup>Q. Huang, R. Liu, G. Lei, H. Huang, J. Li, S. He, D. Li, L. Yan, J. Zhou, and Q. Huang, *J. Nucl. Mater.* **465**, 640 (2015).
- <sup>104</sup>C. Wang, T. Yang, J. Xiao, S. Liu, J. Xue, J. Wang, Q. Huang, and Y. Wang, *Acta Mater.* **98**, 197 (2015).
- <sup>105</sup>C. Wang, T. Yang, J. Xiao, S. Liu, J. Xue, Q. Huang, J. Zhang, J. Wang, Y. Wang, and R. Koc, *J. Am. Ceram. Soc.* **99**, 1769 (2016).
- <sup>106</sup>C. Wang, T. Yang, C.-H. Chen, S. Park, S. Liu, Y. Fang, Z. Yan, J. Xue, J. Zhang, J. Wang, R. C. Ewing, and Y. Wang, *Scr. Mater.* **133**, 19 (2017).
- <sup>107</sup>T. Yang, C. Wang, W. Liu, S. Liu, J. Xiao, Q. Huang, J. Xue, S. Yan, and Y. Wang, *Acta Mater.* **128**, 1 (2017).
- <sup>108</sup>C. Wang, T. Yang, C. L. Tracy, J. Xiao, S. Liu, Y. Fang, Z. Yan, W. Ge, J. Xue, J. Zhang, J. Wang, Q. Huang, R. C. Ewing, and Y. Wang, *Acta Mater.* **144**, 432 (2018).
- <sup>109</sup>T. Yang, C. Wang, W. Liu, S. Liu, J. Xiao, Q. Huang, Y. Wang, and S. J. Zinkle, *J. Nucl. Mater.* **513**, 120 (2019).
- <sup>110</sup>T. Deng, J. Sun, P. Tai, Y. Wang, L. Zhang, H. Chang, Z. Wang, L. Niu, Y. Sheng, D. Xue, Q. Huang, Y. Zhou, P. Song, and J. Li, *Acta Mater.* **189**, 188 (2020).
- <sup>111</sup>W. A. Hanson, M. K. Patel, M. L. Crespillo, F. Zhang, S. J. Zinkle, Y. Zhang, and W. J. Weber, *Acta Mater.* **173**, 195 (2019).
- <sup>112</sup>D. J. Tallman, E. N. Hoffman, E. A. N. Caspi, B. L. Garcia-Diaz, G. Kohse, R. L. Sindelar, and M. W. Barsoum, *Acta Mater.* **85**, 132 (2015).
- <sup>113</sup>J. Ward, S. Middleburgh, M. Topping, A. Garner, D. Stewart, M. W. Barsoum, M. Preuss, and P. Frankel, *J. Nucl. Mater.* **502**, 220 (2018).
- <sup>114</sup>J. Emmerlich, D. Music, P. Eklund, O. Wilhelmsson, U. Jansson, J. M. Schneider, H. Höglberg, and L. Hultman, *Acta Mater.* **55**, 1479 (2007).
- <sup>115</sup>X. H. Wang and Y. C. Zhou, *J. Mater. Chem.* **12**, 2781 (2002).
- <sup>116</sup>H. Zhang, V. Presser, K. G. Nickel, C. Berthold, and Y. Zhou, *J. Am. Ceram. Soc.* **94**, 3460 (2011).

- <sup>117</sup>M. Ghidiu, M. R. Lukatskaya, M. Q. Zhao, Y. Gogotsi, and M. W. Barsoum, *Nature* **516**, 78 (2014).
- <sup>118</sup>M. Naguib, M. Kurtoglu, V. Presser, J. Lu, J. Niu, M. Heon, L. Hultman, Y. Gogotsi, and M. W. Barsoum, *Adv. Mater.* **23**, 4248 (2011).
- <sup>119</sup>H. Zhang, J. Wang, J. Wang, Y. Zhou, S. Peng, and X. Long, *J. Nanomater.* **2013**, 831590.
- <sup>120</sup>H. Fashandi, M. Dahlqvist, J. Lu, J. Palisaitis, S. I. Simak, I. A. Abrikosov, J. Rosen, L. Hultman, M. Andersson, A. Lloyd Spetz, and P. Eklund, *Nat. Mater.* **16**, 814 (2017).
- <sup>121</sup>X. Huang, Y. Feng, Y. Dou, H. Tang, D. Ding, P. Tian, M. Xia, G. Qian, Y. Wang, and X. Zhang, *Scr. Mater.* **113**, 114 (2016).
- <sup>122</sup>M. A. Tunès, R. W. Harrison, S. E. Donnelly, and P. D. Edmondson, *Acta Mater.* **169**, 237 (2019).
- <sup>123</sup>M. Bugnet, V. Mauchamp, P. Eklund, M. Jaouen, and T. Cabioch, *Acta Mater.* **61**, 7348 (2013).
- <sup>124</sup>J. C. Nappé, I. Monnet, P. Grosseau, F. Audubert, B. Guilhot, M. Beauvy, M. Benabdesselam, and L. Thomé, *J. Nucl. Mater.* **409**, 53 (2011).
- <sup>125</sup>D. Hull and D. J. Bacon, *Introduction to Dislocations* (Butterworth-Heinemann, 2001).
- <sup>126</sup>X. Li, Y. Wei, L. Lu, K. Lu, and H. Gao, *Nature* **464**, 877 (2010).
- <sup>127</sup>X. M. Bai, A. F. Voter, R. G. Hoagland, M. Nastasi, and B. P. Uberuaga, *Science* **327**, 1631 (2010).
- <sup>128</sup>M. Bugnet, V. Mauchamp, E. Oliviero, M. Jaouen, and T. Cabioch, *J. Nucl. Mater.* **441**, 133 (2013).
- <sup>129</sup>Q. Huang, H. Han, R. Liu, G. Lei, L. Yan, J. Zhou, and Q. Huang, *Acta Mater.* **110**, 1 (2016).
- <sup>130</sup>D. J. Singh and B. M. Klein, *Phys. Rev. B: Condens. Matter* **46**, 14969 (1992).
- <sup>131</sup>M. Magnusson, M. Andersson, J. Lu, L. Hultman, and U. Jansson, *J. Phys.: Condens. Matter* **24**, 225004 (2012).
- <sup>132</sup>M. K. Patel, D. J. Tallman, J. A. Valdez, J. Aguiar, O. Anderoglu, M. Tang, J. Griggs, E. Fu, Y. Wang, and M. W. Barsoum, *Scr. Mater.* **77**, 1 (2014).
- <sup>133</sup>D. W. Clark, S. J. Zinkle, M. K. Patel, and C. M. Parish, *Acta Mater.* **105**, 130 (2016).
- <sup>134</sup>S. Liu, C. Wang, T. Yang, Y. Fang, Q. Huang, and Y. Wang, *Nucl. Instrum. Methods Phys. Res., Sect. B* **406**, 662 (2017).
- <sup>135</sup>W. A. Hanson, M. K. Patel, M. L. Crespiello, Y. Zhang, and W. J. Weber, *Acta Mater.* **161**, 302 (2018).
- <sup>136</sup>H. Zhang, R. Su, L. Shi, D. J. O'Connor, B. V. King, and E. H. Kisi, *J. Eur. Ceram. Soc.* **38**, 1253 (2018).
- <sup>137</sup>P. Song, J. Sun, Z. Wang, M. Cui, T. Shen, Y. Li, L. Pang, Y. Zhu, Q. Huang, and J. Lü, *Nucl. Instrum. Methods Phys. Res., Sect. B* **326**, 332 (2014).
- <sup>138</sup>H. H. Shen, L. Ao, F. Z. Li, S. M. Peng, H. B. Zhang, K. Sun, and X. T. Zu, *J. Nucl. Mater.* **485**, 262 (2017).
- <sup>139</sup>H. Zhang, R. Su, L. Shi, D. J. O'Connor, and H. Wen, *Appl. Surf. Sci.* **434**, 1210 (2018).
- <sup>140</sup>H. H. Qarra, K. M. Knowles, M. E. Vickers, S. Akhmadaliev, and K. Lambrinou, *J. Nucl. Mater.* **523**, 1 (2019).
- <sup>141</sup>D. J. Tallman, L. He, B. L. Garcia-Diaz, E. N. Hoffman, G. Kohse, R. L. Sindelar, and M. W. Barsoum, *J. Nucl. Mater.* **468**, 194 (2016).
- <sup>142</sup>D. J. Tallman, L. He, J. Gan, E. A. N. Caspi, E. N. Hoffman, and M. W. Barsoum, *J. Nucl. Mater.* **484**, 120 (2017).
- <sup>143</sup>F. Wang, Q. Su, M. Nastasi, M. A. Kirk, M. Li, and B. Cui, *Ceram. Int.* **44**, 14686 (2018).
- <sup>144</sup>S. J. Zinkle and J. T. Busby, *Mater. Today* **12**, 12 (2009).
- <sup>145</sup>S. J. Zinkle, J. P. Blanchard, R. W. Callis, C. E. Kessel, R. J. Kurtz, P. J. Lee, K. A. McCarthy, N. B. Morley, F. Najmabadi, R. E. Nygren, G. R. Tynan, D. G. Whyte, R. S. Willms, and B. D. Wirth, *Fusion Eng. Des.* **89**, 1579 (2014).
- <sup>146</sup>S. J. Zinkle and L. L. Snead, *Annu. Rev. Mater. Res.* **44**, 241 (2014).
- <sup>147</sup>Y. Mo, P. Rulis, and W. Y. Ching, *Phys. Rev. B* **86**, 165122 (2012).
- <sup>148</sup>M. K. Drulis, H. Drulis, S. Gupta, M. W. Barsoum, and T. El-Raghy, *J. Appl. Phys.* **99**, 093502 (2006).
- <sup>149</sup>K. R. Whittle, M. G. Blackford, R. D. Aughterson, S. Moricca, G. R. Lumpkin, D. P. Riley, and N. J. Zaluzec, *Acta Mater.* **58**, 4362 (2010).
- <sup>150</sup>J. Ward, D. Bowden, D. Stewart, M. W. Barsoum, P. Frankel, and M. Preuss, *Scr. Mater.* **165**, 98 (2019).
- <sup>151</sup>D. Bowden, J. Ward, S. Middleburgh, S. de Moraes Shubeita, E. Zapata-Solvias, T. Lapauw, J. Vleugels, K. Lambrinou, W. E. Lee, M. Preuss, and P. Frankel, *Acta Mater.* **183**, 24 (2020).
- <sup>152</sup>S. R. G. Christopoulos, N. Kelaidis, and A. Chroneos, *Solid State Commun.* **261**, 54 (2017).
- <sup>153</sup>K. Trachenko, *J. Phys.: Condens. Matter* **16**, R1491 (2004).
- <sup>154</sup>S. H. Shah and P. D. Bristowe, *Sci. Rep.* **7**, 9667 (2017).
- <sup>155</sup>M. Roknuzzaman, M. A. Hadi, M. J. Abden, M. T. Nasir, A. K. M. A. Islam, M. S. Ali, K. Ostrikov, and S. H. Naqib, *Comput. Mater. Sci.* **113**, 148 (2016).
- <sup>156</sup>Y. C. Zhou, X. H. Wang, Z. M. Sun, and S. Q. Chen, *J. Mater. Chem.* **11**, 2335 (2001).
- <sup>157</sup>O. Knotek, M. Böhmer, and T. Leyendecker, *J. Vac. Sci. Technol., A* **4**, 2695 (1986).
- <sup>158</sup>V. Lipatnikov and A. Gusev, *J. Exp. Theor. Phys. Lett.* **70**, 294 (1999).
- <sup>159</sup>Y. Bai, X. Qi, X. He, D. Sun, F. Kong, Y. Zheng, R. Wang, and A. I. Duff, *J. Am. Ceram. Soc.* **102**, 3715 (2019).
- <sup>160</sup>J. C. Nappé, C. Maurice, P. Grosseau, F. Audubert, L. Thomé, B. Guilhot, M. Beauvy, and M. Benabdesselam, *J. Eur. Ceram. Soc.* **31**, 1503 (2011).
- <sup>161</sup>C. Ang, C. Silva, C. Shih, T. Koyanagi, Y. Katoh, and S. J. Zinkle, *Scr. Mater.* **114**, 74 (2016).
- <sup>162</sup>R. Su, H. Zhang, L. Shi, and H. Wen, *J. Eur. Ceram. Soc.* **39**, 1993 (2019).
- <sup>163</sup>C. L. Tracy, M. Lang, F. Zhang, C. Trautmann, and R. C. Ewing, *Phys. Rev. B* **92**, 174101 (2015).
- <sup>164</sup>C. L. Tracy, J. McLain Pray, M. Lang, D. Popov, C. Park, C. Trautmann, and R. C. Ewing, *Nucl. Instrum. Methods Phys. Res., Sect. B* **326**, 169 (2014).
- <sup>165</sup>L. L. Snead, T. Nozawa, Y. Katoh, T.-S. Byun, S. Kondo, and D. A. Petti, *J. Nucl. Mater.* **371**, 329 (2007).
- <sup>166</sup>C. Ang, S. Zinkle, C. Shih, C. Silva, N. Cetiner, and Y. Katoh, *J. Nucl. Mater.* **483**, 44 (2017).
- <sup>167</sup>D. J. Tallman, J. Yang, L. Pan, B. Anasori, and M. W. Barsoum, *J. Nucl. Mater.* **460**, 122 (2015).
- <sup>168</sup>J. G. Gigax, M. Kennas, H. Kim, T. Wang, B. R. Maier, H. Yeom, G. O. Johnson, K. Sridharan, and L. Shao, *J. Nucl. Mater.* **523**, 26 (2019).
- <sup>169</sup>N. Casal, F. Sordo, F. Mota, J. Jordanova, A. García, A. Ibarra, R. Vila, D. Rapisarda, V. Queral, and M. Perledo, *J. Nucl. Mater.* **417**, 1316 (2011).
- <sup>170</sup>J. Wang, R. Shu, Y. Dong, T. Shao, Q. H. Deng, X. B. Zhou, F. Huang, S. Y. Du, Z. G. Wang, J. M. Xue, Y. G. Wang, and Q. Huang, *Scr. Mater.* **137**, 13 (2017).
- <sup>171</sup>J. Xiao, C. Wang, T. Yang, S. Kong, J. Xue, and Y. Wang, *Nucl. Instrum. Methods Phys. Res., Sect. B* **304**, 27 (2013).
- <sup>172</sup>C. Wang, W. Zhang, Z. Han, and L. Shi, *J. Am. Ceram. Soc.* **101**, 5771 (2018).
- <sup>173</sup>Y. Xu, X. Bai, X. Zha, Q. Huang, J. He, K. Luo, Y. Zhou, T. C. Germann, J. S. Francisco, and S. Du, *J. Chem. Phys.* **143**, 114707 (2015).
- <sup>174</sup>L. L. Snead, *J. Nucl. Mater.* **329–333**, 524 (2004).
- <sup>175</sup>J. C. Nappé, I. Monnet, F. Audubert, P. Grosseau, M. Beauvy, and M. Benabdesselam, *Nucl. Instrum. Methods Phys. Res., Sect. B* **270**, 36 (2012).
- <sup>176</sup>X. M. Liu, M. Le Flem, J. L. Béchade, and I. Monnet, *J. Nucl. Mater.* **401**, 149 (2010).
- <sup>177</sup>N. C. Ghosh and S. P. Harimkar, *Ceram. Int.* **39**, 6777 (2013).
- <sup>178</sup>L. F. Marion and I. Monnet, *J. Nucl. Mater.* **433**, 534 (2013).
- <sup>179</sup>J. Busby, G. Was, and E. Kenik, *J. Nucl. Mater.* **302**, 20 (2002).
- <sup>180</sup>Y. Zhang, T. T. Zuo, Z. Tang, M. C. Gao, K. A. Dahmen, P. K. Liaw, and Z. P. Lu, *Prog. Mater. Sci.* **61**, 1 (2014).
- <sup>181</sup>J. Gild, Y. Zhang, T. Harrington, S. Jiang, T. Hu, M. C. Quinn, W. M. Mellor, N. Zhou, K. Vecchio, and J. Luo, *Sci. Rep.* **6**, 37946 (2016).
- <sup>182</sup>J.-W. Yeh and S.-J. Lin, *J. Mater. Res.* **33**, 3129 (2018).
- <sup>183</sup>P. Singh, D. Sauceda, and R. Arroyave, *Acta Mater.* **184**, 50 (2020).
- <sup>184</sup>W. Bao, X.-G. Wang, H. Ding, P. Lu, C. Zhu, G.-J. Zhang, and F. Xu, *Scr. Mater.* **183**, 33 (2020).
- <sup>185</sup>Y. Li, J. Lu, M. Li, K. Chang, X. Zha, Y. Zhang, K. Chen, P. O. A. Persson, L. Hultman, P. Eklund, S. Du, J. S. Francisco, Z. Chai, Z. Huang, and Q. Huang, *Proc. Natl. Acad. Sci. U.S.A.* **117**, 820 (2020).
- <sup>186</sup>T. Yang, C. Li, S. J. Zinkle, S. Zhao, H. Bei, and Y. Zhang, *J. Mater. Res.* **33**, 3077 (2018).
- <sup>187</sup>Q. Tao, J. Lu, M. Dahlqvist, A. Mockute, S. Calder, A. Petruhins, R. Meshkian, O. Rivin, D. Potashnikov, E. A. N. Caspi, H. Shaked, A. Hoser, C. Opagiste, R.-M. Galera, R. Salikhov, U. Wiedwald, C. Ritter, A. R. Wildes, B. Johansson,

- L. Hultman, M. Farle, M. W. Barsoum, and J. Rosen, *Chem. Mater.* **31**, 2476 (2019).
- <sup>188</sup>A. Champagne, O. Chaix-Pluchery, T. Ouisse, D. Pinek, I. Gélard, L. Jouffret, M. Barbier, F. Wilhelm, Q. Tao, J. Lu, J. Rosen, M. W. Barsoum, and J. C. Charlier, *Phys. Rev. Mater.* **3**, 053609 (2019).
- <sup>189</sup>A. Petruhins, J. Lu, L. Hultman, and J. Rosen, *Mater. Res. Lett.* **7**, 446 (2019).
- <sup>190</sup>A. Champagne, F. Ricci, M. Barbier, T. Ouisse, D. Magnin, S. Ryelandt, T. Pardoen, G. Hautier, M. W. Barsoum, and J. C. Charlier, *Phys. Rev. Mater.* **4**, 013604 (2020).
- <sup>191</sup>X. Bai, Q. Deng, Y. Qiao, N. Qiu, X. Zha, J. Zhou, K. Luo, Y. Zhou, Q. Huang, and S. Du, *Ceram. Int.* **44**, 1646 (2018).
- <sup>192</sup>R. C. Ewing, J. Lian, and L. M. Wang, *MRS Proc.* **792**, R2.1 (2011).
- <sup>193</sup>J. Wang, S. Liu, D. Ren, T. Shao, P. Eklund, R. Huang, Y. Zhu, F. Huang, S. Du, Z. Wang, J. Xue, Y. Wang, and Q. Huang, *J. Nucl. Mater.* **509**, 181 (2018).
- <sup>194</sup>M. Griffiths, *J. Nucl. Mater.* **159**, 190 (1988).
- <sup>195</sup>X. Zhou, Y.-H. Han, X. Shen, S. Du, J. Lee, and Q. Huang, *J. Nucl. Mater.* **466**, 322 (2015).
- <sup>196</sup>T. Koyanagi, Y. Katoh, T. Nozawa, L. L. Snead, S. Kondo, C. H. Henager, M. Ferraris, T. Hinoki, and Q. Huang, *J. Nucl. Mater.* **511**, 544 (2018).
- <sup>197</sup>M. Li, X. Zhou, H. Yang, S. Du, and Q. Huang, *Scr. Mater.* **143**, 149 (2018).
- <sup>198</sup>X. Zhou, Z. Liu, Y. Li, Y. Li, P. Li, F. Huang, S. Ding, J. Lee, S. Du, and Q. Huang, *Ceram. Int.* **44**, 15785 (2018).
- <sup>199</sup>X. Zhang, Y. Li, Y. Qiao, H. Chen, Y. Wang, T. C. Germann, Q. Huang, X. Bai, X. Zhou, Y. Guo, K. Luo, and S. Du, *J. Phys. Chem. Solids* **127**, 119 (2019).
- <sup>200</sup>Y. Katoh, L. L. Snead, T. Cheng, C. Shih, W. D. Lewis, T. Koyanagi, T. Hinoki, C. H. Henager, and M. Ferraris, *J. Nucl. Mater.* **448**, 497 (2014).
- <sup>201</sup>Y. Gogotsi and B. Anasori, *ACS Nano* **13**, 8491 (2019).
- <sup>202</sup>Y. Li, H. Shao, Z. Lin, J. Lu, L. Liu, B. Dupoyer, P. O. A. Persson, P. Eklund, L. Hultman, M. Li, K. Chen, X. H. Zha, S. Du, P. Rozier, Z. Chai, E. Raymundo-Pinero, P. L. Taberna, P. Simon, and Q. Huang, *Nat. Mater.* **19**, 84 (2020).
- <sup>203</sup>W. Hong, B. C. Wyatt, S. K. Nemanic, and B. Anasori, *MRS Bull.* **45**, 850 (2020).
- <sup>204</sup>Z. Guo, J. Zhou, L. Zhu, and Z. Sun, *J. Mater. Chem. A* **4**, 11446 (2016).
- <sup>205</sup>Y. Bai, K. Zhou, N. Srikanth, J. H. Pang, X. He, and R. Wang, *RSC Adv.* **6**, 35731 (2016).
- <sup>206</sup>T. Ito and S. Okazaki, *Nature* **406**, 1027 (2000).
- <sup>207</sup>S. Shukla, S.-Y. Kang, and S. Saxena, *Appl. Phys. Rev.* **6**, 021311 (2019).
- <sup>208</sup>Z. Li and F. Chen, *Appl. Phys. Rev.* **4**, 011103 (2017).
- <sup>209</sup>S. Kota, E. Zapata-Solvias, A. Ly, J. Lu, O. Elkassabany, A. Huon, W. E. Lee, L. Hultman, S. J. May, and M. W. Barsoum, *Sci. Rep.* **6**, 26475 (2016).
- <sup>210</sup>A. Larionov, L. Chekushina, and E. Suslov, in *Development and Investigation of High-Strength Neutron-Absorbing Composite Coatings Based on Borides of Metals* (Trans Tech Publications, 2019), p. 660.
- <sup>211</sup>H. Zhang, J. Y. Kim, R. Su, P. Richardson, J. Xi, E. Kisi, J. O'Connor, L. Shi, and I. Szlufarska, *Acta Mater.* **196**, 505 (2020).